UNIVERSIDADE D
COIMBRA

Diego Garcia dos Santos

MUONIUM AS A MODEL FOR HYDROGEN IN SOLAR CELL ABSORBERS CIGS AND CZTS

Dissertação no âmbito do Mestrado em Física, especialidade de Física da Matéria Condensada, orientado pelo Professor Doutor Rui César do Espírito Santo Vilão e apresentada ao Departamento de Física da Faculdade de Ciências e Tecnologia

Setembro de 2023

Acknowledgments

I would first like to thank my Lord and Savior, Jesus Christ, for the breath of life he breathes into my nostrils every morning. I thank my wife, Valéria dos Santos, for all her support, love, and care, without whom I would not have made it this far. Thanks to Professor Rui César do Espírito Santo Vilão for his extreme patience with me and all his attention.

Resumo

Nesta dissertação apresentamos medidas de espetroscopia de spin de muões (μSR) nos semicondutores do tipo calcopirite $Cu_2ZnSnSe_4$(CZTS) e $Cu(In_{0.79}Ga_{0.21})_{1.09}Se_{2.1}$(CIGS), utilizados como absorvedores em células solares de filme fino. O átomo exótico de muónio, formado por um muão positivo e um eletrão, foi utilizado como pseudo-isótopo leve do hidrogénio, a fim de simular o comportamento da impureza de hidrogénio, omnipresente nestes materiais. Foram analisados e elaborados modelados físicos relativamente aos resultados de experiências realizadas no instrumento EMU da instalação ISIS no Laboratório Rutherford Appleton no Reino Unido, implantando muões positivos de 4 MeV em amostras policristalinas.

Foi assim realizada uma caraterização completa das configurações do muónio. As medições em campo magnético nulo permitiram uma separação clara das distintas componentes do espetro μSR. Medidas de repolarização em geometria de campo longitudinal permitiram avaliar a interação hiperfina dos estados do muónio, que se verificou corresponder a um estado compacto quase atómico (1.6 GHz). As configurações equivalentes de muónio dos estados de impureza dadora e aceitadora de hidrogénio, previstas teoricamente, foram assim caracterizadas como muónio intersticial e muónio ligado, respetivamente, e a sua estabilidade térmica foi investigada por medidas de dependência com a temperatura. Foi também caracterizada uma componente de relaxação rápida associada a um estado transitório no processo de termalização, através de medições dependentes do campo em geometria transversal. No entanto, a configuração dominante nestas medidas de espetroscopia do muão positivo é uma componente sem relaxação de spin, que associamos a muões que param em defeitos ou perto deles.

Abstract

In this dissertation we present muon spin spectroscopy (μSR) measurements in the chalcopyrite solar cell semiconductor absorbers $Cu_2ZnSnSe_4$(CZTS) and $Cu(In_{0.79}Ga_{0.21})_{1.09}Se_{2.1}$(CIGS). The exotic muonium atom, consisting of a positive muon and an electron, was used as a light pseudo-isotope of hydrogen, in order to model the behavior of the omnipresent hydrogen impurity in these materials. The results of experiments performed at the EMU instrument in the ISIS Facility of the Rutherford Appleton Laboratory in the United Kingdom by implanting 4 MeV positive muons in polycrystalline samples, were analyzed and modeled.

A thorough characterization of the muonium configurations was therefore performed. Measurements in zero applied magnetic fields allowed for a clear separation of the distinct components of the μSR spectrum. Repolarization measurements in the longitudinal field geometry allowed to assess the hyperfine interaction of the muonium states, which was found to correspond to an atomic-like value (1.6 GHz). The equivalent muonium configurations of the theoretically predicted hydrogen donor and acceptor impurity states were therefore characterized as interstitial muonium and bound muonium, respectively, and their thermal stability was investigated by temperature dependence measurements. A fast relaxing component associated to a transient state in the thermalization process has also been characterized, by field-dependent measurements in transverse geometry. However, the dominant configuration is a non-relaxing component that we associate to muons stopping at or near defects.

List of tables

List of figures

Contents

Chapter 1: Photovoltaic Solar Cells

1.1 Why Photovoltaic Technologies?

The rise in energy consumption is a direct consequence of the increasing population. Currently, most of this energy is obtained by burning fossil fuels (as illustrated in Fig. 1.1), which not only causes severe pollution due to the release of high levels of carbon dioxide (CO_2) into the atmosphere but is also becoming scarcer with time. Thus, the focus is shifting towards renewable energy sources, like solar energy, an inexhaustible and environmentally friendly energy source. It is essential to recognize that although fossil fuels remain the primary source of energy extraction (Fig. 1), there is a growing trend of investments in renewable energies. According to the International Energy Agency's report on global energy investment for 2023, the investment in non-polluting energy has surpassed that in fossil fuels. Specifically, from 2021 to 2023, 24% of the acquisition was devoted to non-polluting energy, while only 15% was allocated to fossil fuels (Fig. 1.2).

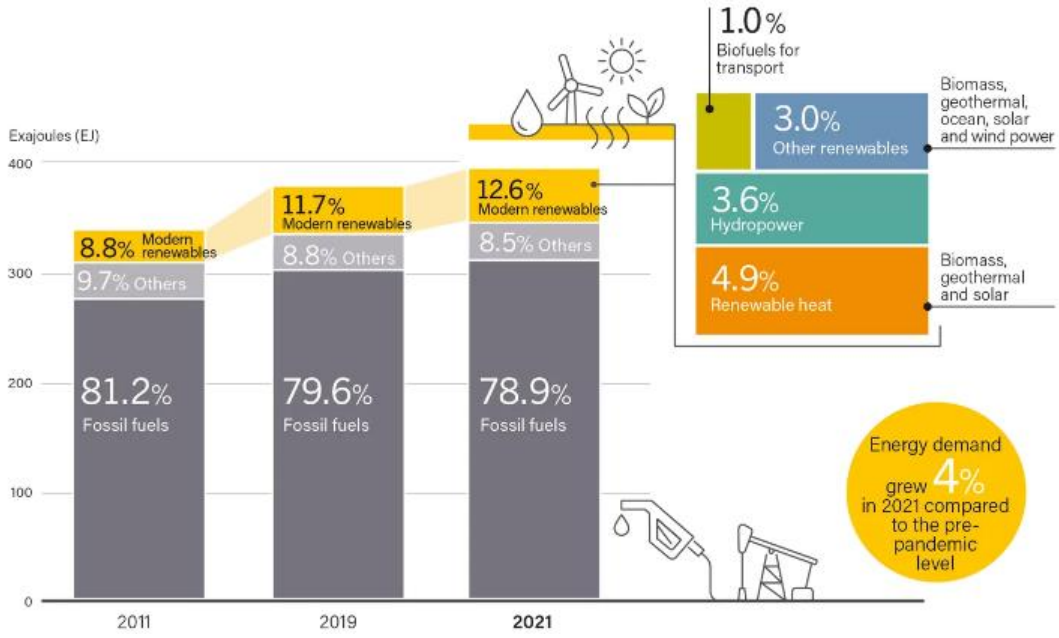

Figure 1.1: : The data shows the total energy consumption by source in 2011, 2019, and 2021 (From [REN21]).

The power sector has greatly benefited from the substantial investment in clean energy, particularly in photovoltaic solar cells, also referred to as PV solar cells (Fig.1.3). The basic operating principle of these devices is transforming solar energy into electrical power. These devices use solar energy as an infinite fuel source, are environmentally friendly, cost-effective to operate, can be seamlessly integrated into building structures, and function at room

temperature [Luq11]. They have numerous applications, including powering electrical equipment, electric vehicles [Fac+20], irrigation systems [Gar+19], and space applications [Ban+20].

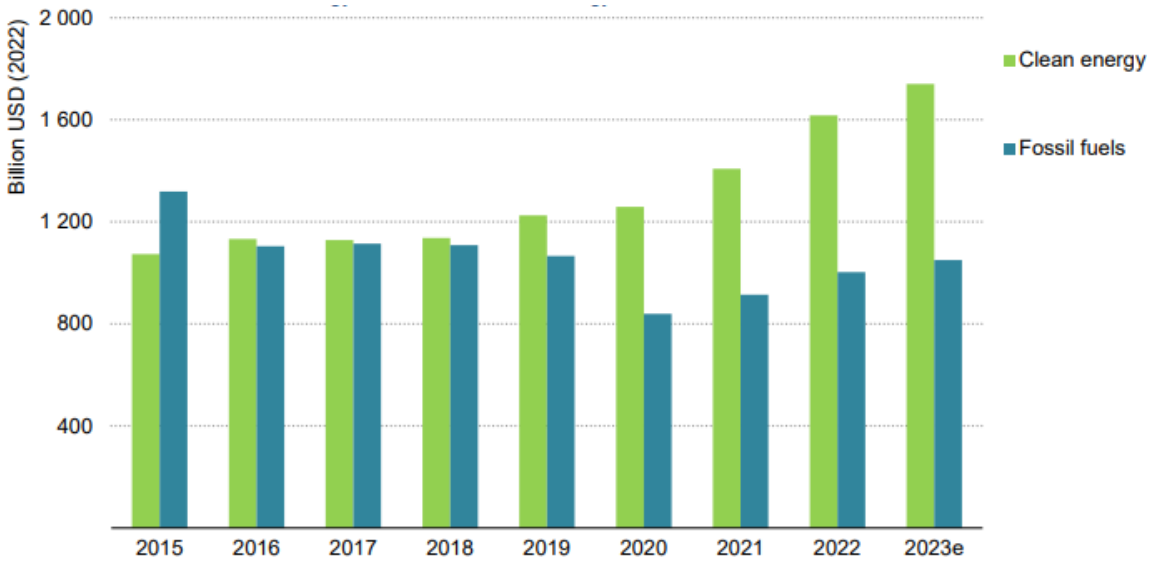

Figure 1.2: Investment in clean energy versus fossil fuels on a global scale. The term "2023e" refers to the estimated values for the year 2023 (From [IEA]).

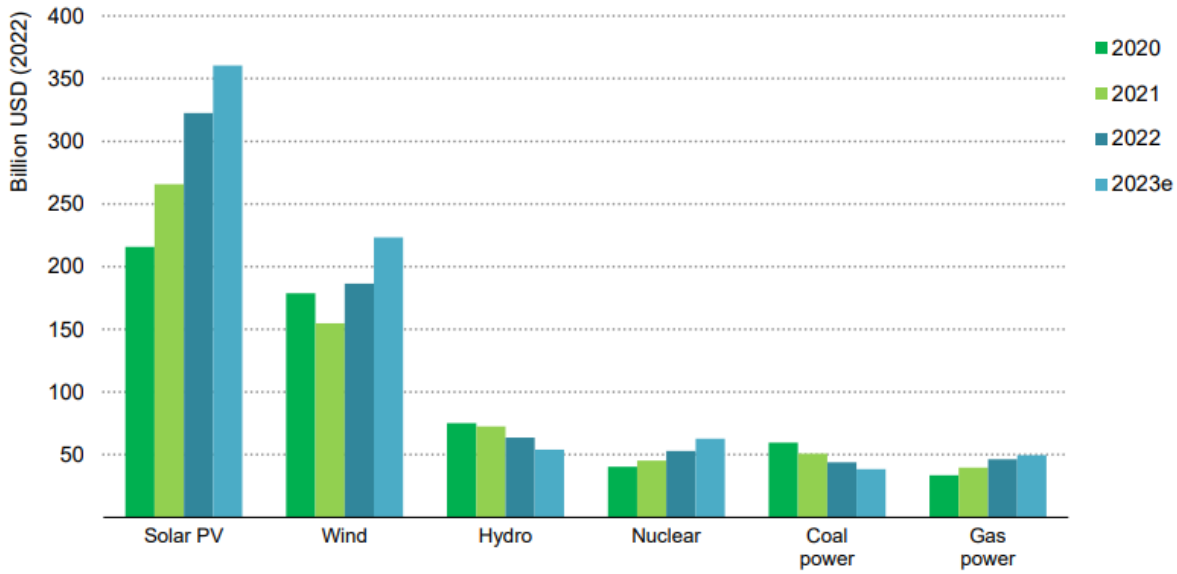

Figure 1.3:Yearly investment in power generation for specific technologies on a global scale. The term "2023e" refers to the estimated values for the year 2023 (From [IEA]).

This chapter aims to bring attention to the crucial aspects of solar cells, focusing on thin-film solar cells. The main topic of discussion will be copper indium gallium di-selenide ($CuIn_xGa_{1-x}Se_2$, or CIGS) and copper zinc tin sulfide or selenide ($Cu_2ZnSn(S, Se)_4$, or CZTSSe) thin films.

1.2 An Overview of CIGS and CZTS

There are two categories of photovoltaic cells: wafer-based and thin-film-based (Fig. 1.4). The crystalline silicon solar cell (c-Si), which falls into the wafer-based group, is the most widely used type, accounting for around 90% [Kim+21] of total production in the solar cell market. However, silicon solar cells have a high production cost due to the high degree of silicon purity required for a cell's optimal performance [Liu+20]. Thin films use fewer raw materials, lowering production costs compared to wafer-based solar cells. As an illustration, silicon requires approximately 200 microns to efficiently absorb incoming light, whereas a thin film only needs a few microns of thickness. As a result of this small thickness, for mechanical stability, thin films are deposited on glass, metal, or plastic (polymer) substrates. Due to its low cost, flexibility, and lightweight, the latter allows the production of flexible and portable solar panels [Li+21]. Some companies are already marketing flexible CIGS thin-film solar panels with power values ranging from 100 to 200 Watts [BOU]. Currently, CZTS thin films are not available for commercial purchase. However, they are a promising option for manufacturing flexible substrates [Li+21].

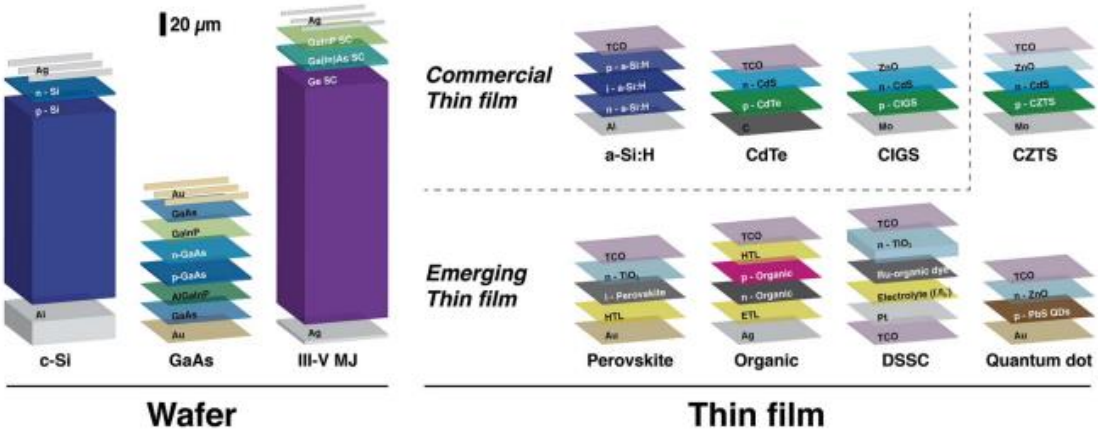

Figure 1.4: Typical solar PV device structures, divided into wafer-based and thin-film technologies. Thicknesses are shown to scale (From [Liu+20]).

Over time, CIGS materials have gained popularity due to their increasing power conversion efficiency (Fig. 1.5). They are currently at the forefront of the thin film photovoltaics market, with the highest efficiency value of 23.6% [NRE]. In contrast, the efficiency of CZTS materials is 14.9% [NRE], much smaller than 23.6%, making them impractical for commercial production. Thus, they are considered emerging thin films (Fig. 1.4). However, due to the In and Ga sources scarcity, CZTS is regarded as a viable alternative to CIGS since Zn and Sn are earth-abundant elements, nature-friendly, and cheaper [Reg+21]. The raw material cost, expressed in cents per watt (¢/W), of CZTS can be up to five times less than that of CIGS (Figure 1.6).

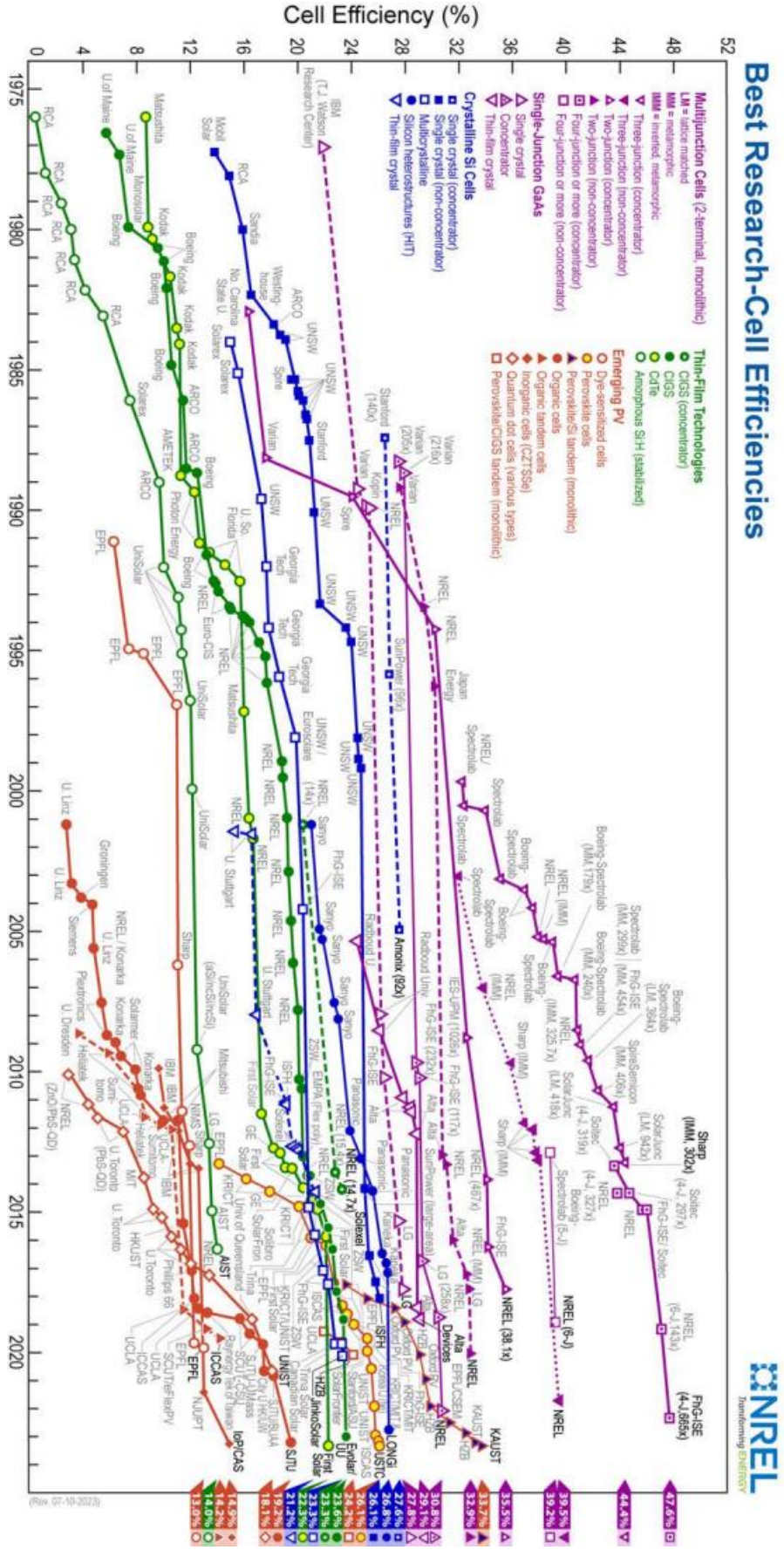

Figure 1.5: Summary of the progress made in solar cell efficiency over the years, including the highest efficiencies achieved to date (From [NRE]).

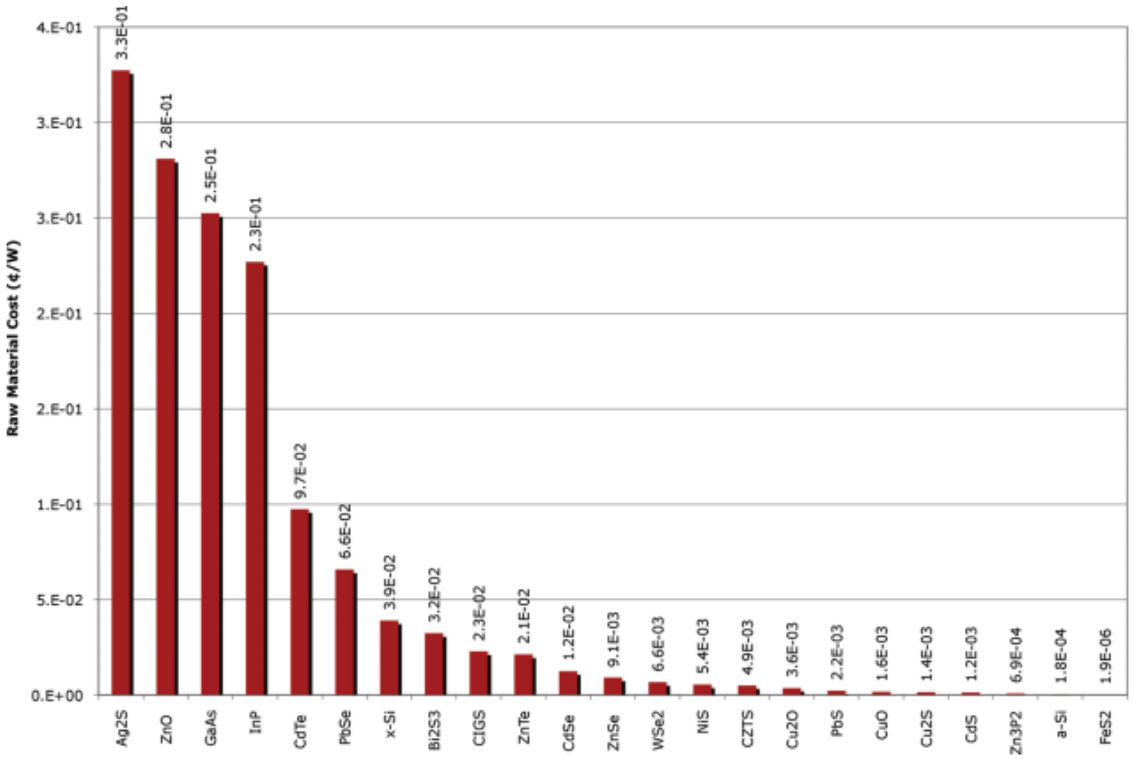

Figure 1.6: Minimum ¢/W for 23 inorganic photovoltaic materials. Component cost contribution in ¢/W is a strong indicator of value for future deployment. Calculated values for all 23 compounds, including CIGS and CZTS, are displayed (From [Wad09]).

1.3 The operating mechanism of a photovoltaic solar cell.

The primary working component of a solar cell is the so-called p-n junction (Fig. 1.6). It is a single semiconductor crystal doped so that one region is an n-type material (excess of electrons), and the adjacent region is a p-type material (excess of holes). Due to the concentration gradients of electrons and holes, diffusion currents take place. Electrons near the p-n junction diffuse across it from the n-side to the p-side, making the n-zone near the junction positively charged (donors lose their valence shell electron, becoming positively charged ions). Similarly, the holes near the junction diffuse across it from the p-side to the n-side, making the p-zone near the junction negatively charged (acceptors are ionized and become negatively charged). This process of separating charge carriers creates an electric field near the p-n junction that exactly balances the diffusion and drag currents, leading to a zero net current across the junction. As a result of this field, holes, and electrons are essentially swept away from the p-n area, giving rise to the so-called depletion region or space charge region (Fig.1.6).

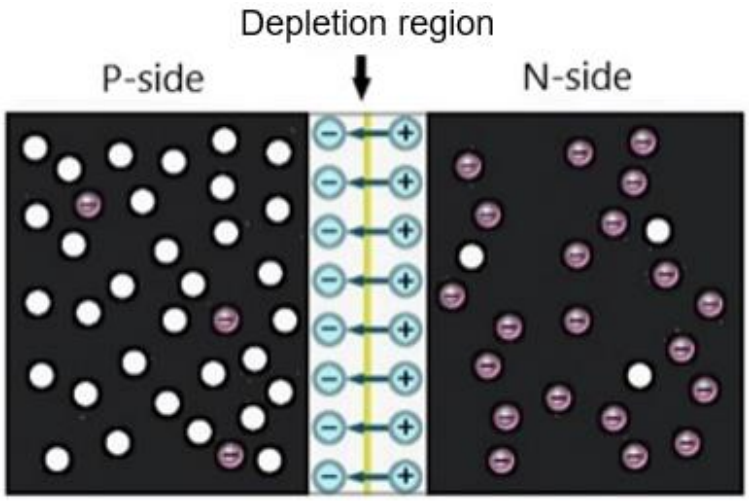

Figure 1.7: Representation of a p-n junction in thermal equilibrium. The p side corresponds to an excess of holes, and the n side to an excess of electrons. The green arrows represent the direction of the electric field produced in the depletion region (Modified from [Al+22]).

In the Fig. 1.8, the essential composition of a solar cell is depicted. A p-n junction is subjected to an external voltage by means of two conductive contacts. The top contact (facing the light) must be transparent to maximize light absorption in the depletion zone. Similarly, the "top" semiconductor of the junction must be thin (as must the corresponding depletion zone), which implies high doping.

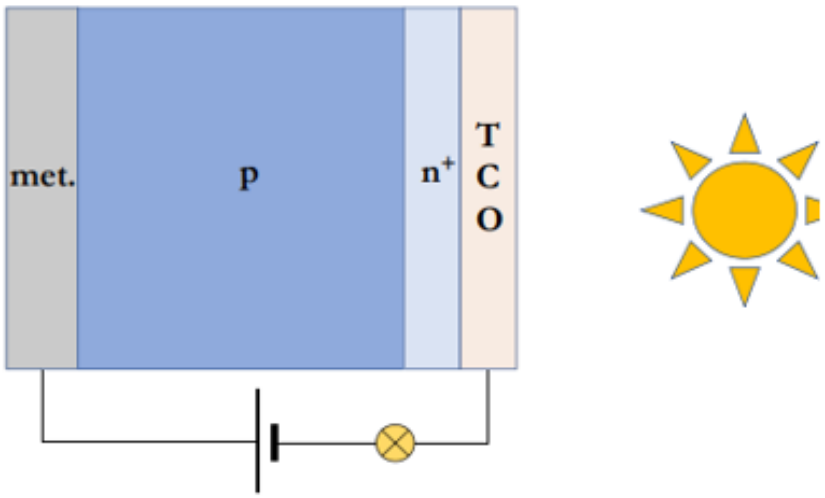

Figure 1.8: Schematic diagram of a solar cell based on an n^+-p semiconductor junction subject to an applied voltage. n^+ means high doping. The electrical contacts are typically metallic, but a transparent conductive oxide (TCO) can advantageously replace the metal in the case of external contact (From [Vil22]).

The basic operating principle of a solar cell is based on the creation of electron-hole pairs in the depletion zone from the absorption of photons. The electric field then rapidly separates these pairs, sending the holes into the p zone and the electrons into the n zone. This process generates

a photocurrent J_L that flows from n to p. It is important to mention that when the solar cell is not under illumination, the net current flowing through the p-n junction is given by the so-called diode equation:

$$J_D = J_S\left[\exp\left(\frac{eV_{ext}}{kT}\right) - 1\right]. \tag{1.1}$$

J_D represents the diode current. The saturation current is referred to as J_S. V_{ext} stands for the external voltage. Additionally, k represents the Boltzmann constant, e signifies the electron charge, and T indicates the temperature in kelvin. Figure 1.9 shows the behavior of the current J_D as a function of the external voltage V_{ext} applied to the unlit p-n junction.

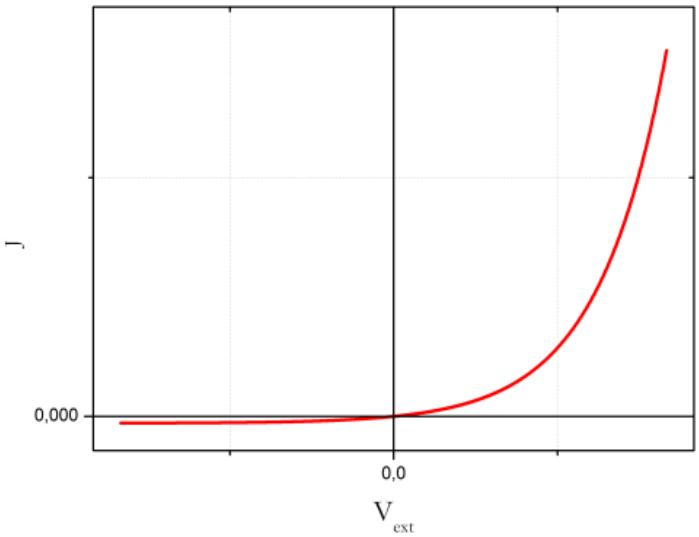

Figure 1.9: I - V curve of a p - n junction subject to an external voltage Vext (From [Vil22]).

The net electric current flowing through the ideal solar cell when operating under illumination can be expressed as:

$$J = J_D - J_L = J_S\left[\exp\left(\frac{eV_{ext}}{kT}\right) - 1\right] - J_L\,, \tag{1.2}$$

where J_L is the photocurrent. Therefore, the basic effect on the I - V curve (Fig. 1.9) consists of the appearance of a negative J_L photocurrent and the corresponding shifting of the I - V curve in the direction of the negative currents (Fig. 1.10).

The maximum power that can be extracted from the ideal cell corresponds to the maximum value $P_m = V_m I_m$ for $V_{ext} = V_m$. The pair (V_m, I_m) defines a (maximum) area on the I - V curve (shown in Figure 1.10). A parameter usually used to estimate the optimal operation of the cell

corresponds to the ratio of this area to the area defined by the pair (V_{oc}, I_{sc}) (and which circumscribes the I - V curve). This ratio is called the Fill Factor:

$$FF = \frac{V_m I_m}{I_{sc} V_{oc}}. \tag{1.3}$$

The efficiency of a solar cell is defined as the ratio of maximum power, P_m, to incident power P_{in}:

$$\eta = \frac{p_m}{p_{in}} = \frac{FFV_{oc}I_{sc}}{p_{in}}. \tag{1.4}$$

The incident power is determined by the properties of the light spectrum incident upon the solar cell.

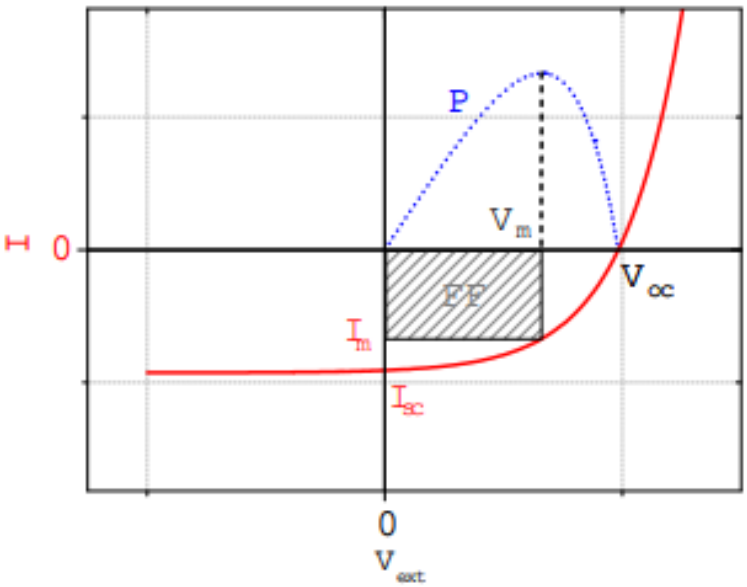

Figure 1.10: The main engineering parameters of a solar cell are shown in its I - V curve, including short circuit current I_{sc}, open circuit voltage V_{oc}, maximum voltage V_m, and maximum current I_m. The power variation with respect to applied voltage is shown in the blue dotted curve (From [Vil22]).

1.4 Hydrogen in CIGS and CZTS

Hydrogen is bound to have an important role in the efficiency of solar cells base on CZTS and CIGS, due to its easy incorporation during the growth process, leading to high concentrations and impact on the functioning and degradation of the devices [Och+00, Sal+11, Yok+10, Bar+10, Var+18]. The understanding of the role of hydrogen in the properties of CZTS is crucial to optimize the performance of these thin film based solar cells. This dissertation is dedicated to a fundamental investigation of the role of hydrogen in these chalcopyrite absorbers, using the positive muon as a light pseudo isotope of hydrogen. Muon spin spectroscopy (μSR) will be used as experimental tool.

Chapter 2: The μSR technique.

2.1 Introduction

In order to have a proper discussion about the μSR technique or muon spectroscopy, it is essential first to understand the nature of muons and their fundamental properties. Furthermore, this discussion will include some examples of scientific applications of this technique.
Muons are unstable elementary particles generated by cosmic rays colliding with Earth's atmosphere or produced through particle accelerators. Cosmic-ray muons have the potential to uncover the inner composition of massive geologic structures, including the upper portion of a volcano [Nag+95, Tan19]. On the other hand, muons generated in particle accelerators are used to conduct condensed matter studies because of their controllability. Muons can have either a negative or positive charge, positive muons being the antiparticle of negative muons. They have an average lifetime of 2.2 μs and a spin of 1/2. Since they have a mass that falls between that of an electron and a proton, the positive muon behaves like a light proton, while the negative muon behaves like a heavy electron. Due to their intense magnetic moment, muons are an excellent choice for magnetic probes. Table 1 illustrates the fundamental properties distinguishing electrons, muons, and protons.

	charge	spin	mass	moment	$\gamma/2\pi$ (MHz T^{-1})	lifetime (μs)
e	$\pm e$	1/2	m_e	$657\mu_p$	28,000	$> 10^{40}$
μ	$\pm e$	1/2	$207m_e$	$3.18\mu_p$	135.5	2.197
p	$\pm e$	1/2	$1836m_e$	μ_p	42.6	$> 10^{42}$

Table 2.1: The properties of the electrons, muons, and protons (sourced from [Ber+12])

As previously mentioned, muons can be either positive or negative. However, most studies on condensed matter using muon spectroscopy primarily rely on the positive muon μ^+. This is due to its higher production rates and because its polarization is maintained during implantation into the sample, unlike the negative muon μ^-, which is affected by spin-orbit coupling [Hil+22]. However, because of spin-orbit coupling mechanisms, negative muons are helpful in determining the chemical composition of materials [Hil+16].

Muon particles have a wide range of scientific applications [Blu+22]. Some examples include detecting magnetic order [Ghe+20], examining the presence of spin fluctuations [Bis+23], determining the penetration depth in superconductors [Kha+23], measuring the local electronic environment in semiconductors (where muons simulate proton impurities) [Mar+21], and conducting a non-destructive elemental analysis of archaeological artifacts [Cat+22]. These are just a few of the many ways in which muons can be utilized for scientific research.

2.2 Muon production

In Section 2.1, it was determined that muons can be classified as either positive or negative. This dissertation focuses on positive muons; all experiments were conducted using this type. This discussion on muon production will exclusively concentrate on positive muons, commonly called "muons" within the μSR community.

The production of muons in particle accelerators involves a two-step process. Firstly, high-energy protons (p), typically about 800 MeV, collide with a target made of carbon or beryllium. This nucleon-nucleon interaction leads to a pion (π^+) being born. The following scheme outlines the process of pion formation:

$$p + p \rightarrow p + n + \pi^+ \tag{2.1}$$

where (n) is a neutron.
Subsequently, the pion, which has a lifetime of 26 ns and has spin equal to zero, disintegrates in a two-body decay, via weak interaction into a muon (μ^+) and a muon neutrino (ν_μ).

$$\pi^+ \rightarrow \mu^+ + \nu_\mu \tag{2.2}$$

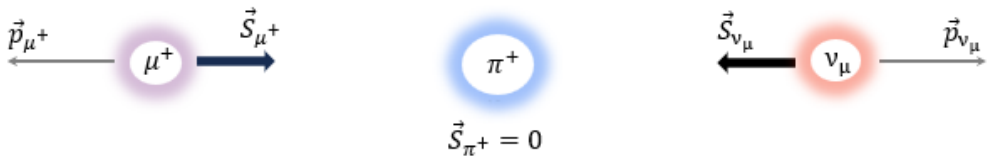

Figure 2.1: Decay of pion in its rest reference frame.

In the rest frame of the pion, immediately after it decays, the muon and neutrino possess equal and opposite linear momenta due to momentum conservation. Concomitantly, there is angular momentum conservation since the pion has spin-zero and parity violation enforces that neutrinos have a definite negative helicity, i.e., spin and momentum are antiparallel (this violation is a weak interaction peculiarity). Thus, since the pion has spin-zero, the muon must also have a negative helicity because of the conservation of angular momentum. As a consequence of both conservation of linear momentum and angular momentum in the rest frame of the pion, the muon and neutrino come out in opposite directions and must have contrary spins (Fig. 2.1). As a result, in the π^+ decay, the muons invariably become 100 % spin-polarized and have a definite energy of 4.1 MeV. This invariance makes generating a beam of totally polarized muons possible.

The muon interacts with its surroundings through a magnetic field during implantation in a condensed matter sample. This environment may originate from the sample itself, an external source (magnetic coils), or both. Consequently, the muon spin performs a Larmor precession about magnetic field B with the angular frequency ω (Fig. 2.2)

$$\omega = \gamma B \tag{2.3}$$

where the gyromagnetic ratio is $\gamma = 2\pi \times 135.5\ \mathrm{MHz/T}$.

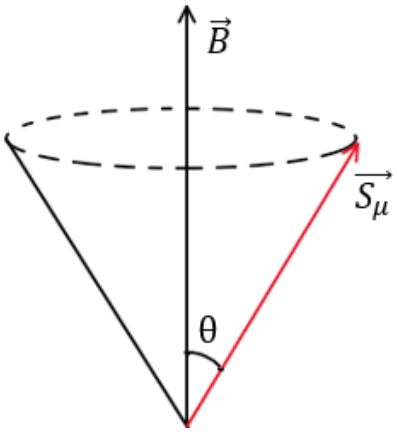

Figure 2.2: Schematic representation of the muon spin precession around a magnetic field. The muon's spin forms an θ angle with the direction of the magnetic field and describes a cone around this field.

2.2.1 Muon decay

The muon has an average lifetime of 2.2μs. In its rest frame, it decays through the weak force into a positron (e^+), an electron neutrino (ν_e), and a muon antineutrino ($\bar{\nu}_\mu$) through the following three-body reaction (Fig. 2.3)

$$\mu^+ \rightarrow e^+ + \nu_e + \bar{\nu}_\mu \tag{2.4}$$

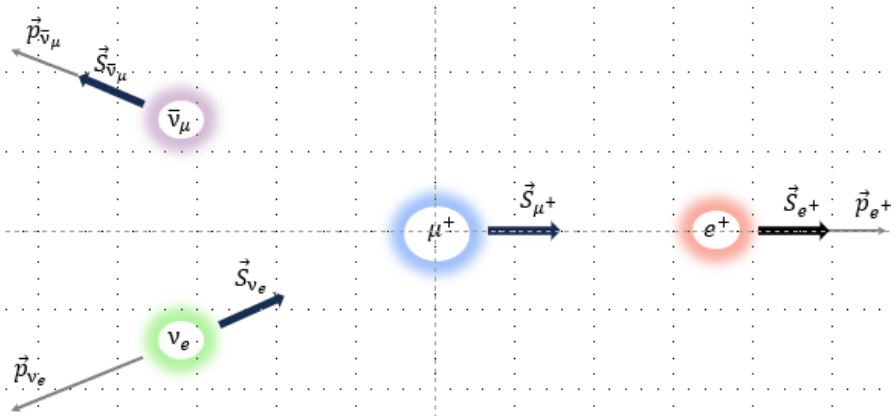

Figure 2.3: Schematic representation of the muon decaying in its rest frame into a positron, neutrino, and antineutrino. The parity violation forces the positron to exit in the same direction as the muon's spin.

Based on the parity violation effect, positron emission is more likely to occur in the same direction as the muon's spin, resulting in an asymmetric emission. The following formula provides positron angular distribution:

$$\Gamma(\theta) = 1 + a(\varepsilon)\cos\theta. \tag{2.5}$$

Here, θ is the angle between the direction of the e^+ emission and the spin of the μ^+. $a(\varepsilon)$ is the asymmetry or anisotropic parameter, which measures the degree of anisotropy of the muon emission. This parameter depends on the normalized energy ε of the positrons as follows

$$a(\varepsilon) = \frac{2\varepsilon - 1}{3 - 2\varepsilon}. \tag{2.6}$$

Where $\varepsilon = E/E_{max}$ corresponds to the energy of the positron normalized to the maximum energy $E_{máx}$ = 53 MeV.

Fig. 2.3 shows the angular distribution (Eq.2.5) for eleven values of the parameter a. For the maximum energy value (53 Mev), a = 1 and the positron has a maximum probability of being emitted in the direction of the muon's spin. On the other hand, for energy that corresponds to half the maximum (26 Mev), the asymmetry disappears, i.e., a = 0. As a result, emissions have an equal chance of occurring in all directions. Considering all energy values, the average asymmetry is ⟨a⟩ = 1/3 (yellow line).

Section 2.3 shows that the tendency of positrons to decay in the direction of muon spin plays a role in how μ^+ interacts with its environment.

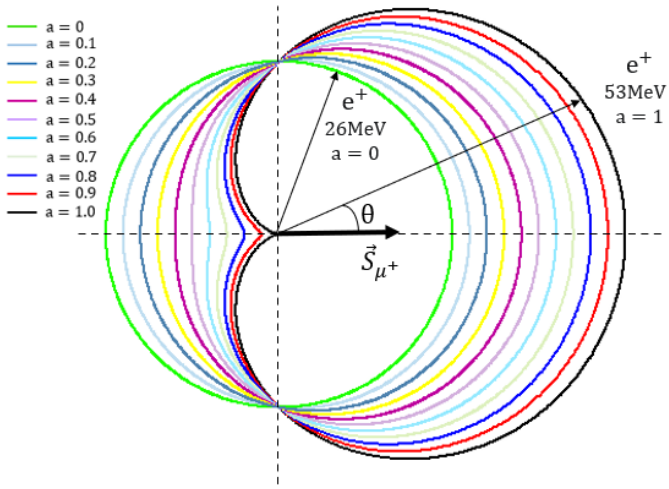

Figure 2.4*:* Angular distribution Γ(θ) of positrons from muon decay for eleven values of parameter a.

2.3 The technique

The diagram in Figure 2.5 illustrates the arrangement of a μSR experiment setup. Before its implantation, the muon μ^+ first passes through a detector (M) that records its arrival time, t_0, using an electronic clock. Afterward, it stops inside the sample. Its spin then undergoes precession after interacting with a magnetic field. The muon subsequently decays by emitting a positron e^+, preferentially in the direction of the μ^+ spin. At a time $t > t_0$, either the forward (F) or the backward (B) detectors sense this emission. The clock then stops, resulting in the recording of an e^+ event. $N_F(t)$ and $N_B(t)$ symbolize the number of e^+ events that the F and B detectors record over time, respectively. Hence,

$$N_{F,B}(t) = N^0_{F,B} e^{-t/\tau_\mu}[1 \mp a_0 P(t)] \tag{2.7}$$

where $\mp$ denotes forward and backward detectors, respectively. $N^0_{F,B}$ is the initial number of positron events in both detectors, τ_μ is the muon average lifetime, a_0 is the initial asymmetry, t is the time interval between muon implantation and the positron detection, and $P(t)$ is the polarization of the muon spin.

The preference for positrons to emerge in the direction of the muon's spin leads to an imbalance in e^+ detection ($N_F(t) \neq N_B(t)$). That being so, it is possible to use this property to monitor how the muon's spin evolves over time using the asymmetric signal A(t) (Eq.2.8).

$$A(t) = \frac{N_F(t) - N_B(t)}{N_F(t) + N_B(t)} \tag{2.8}$$

Assuming detectors with flawless efficiency and geometry and disregarding natural background radiation influences like cosmic muons, Equation 2.8 becomes.

$$A(t) = a_0 P(t) \tag{2.9}$$

If the detectors are not perfectly centered around the sample, or have different efficiencies, it may happen that there is an increase in positron counts due to these purely instrumental reasons. However, this instrumental effect can be easily assessed by measurements under an applied magnetic field perpendicular to the direction of the muon spin: the corresponding time oscillation of the asymmetry can be described by

$$A(t) = \frac{N_F(t) - \alpha N_B(t)}{N_F(t) + \alpha N_B(t)} \tag{2.10}$$

The parameter α in Eq. 2.10 describes the instrumental effect and can be determined by forcing the time average of the asymmetry in Eq. 2.10 to be zero. The anisotropic nature of the emission of positrons is a preponderant factor in determining the evolution of the muon's spin inside the sample through its polarization function. This function plays an essential role in determining the characteristics of the material in question. The type of material and the muon's interaction with its surroundings determine different asymmetric signals.

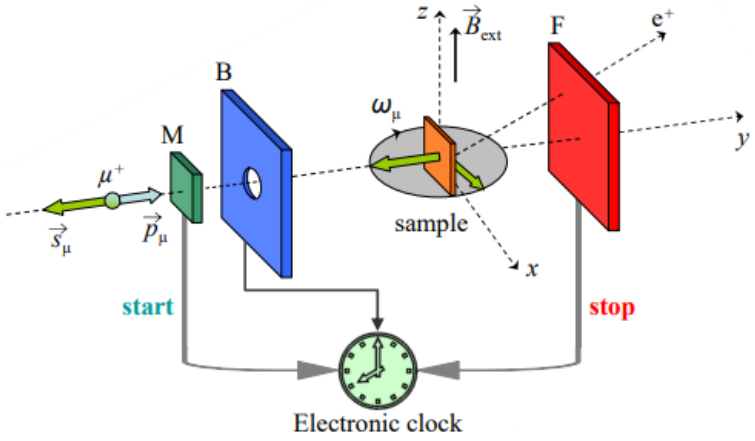

Figure 2.5: Illustration of an experimental setup for conducting muon spectroscopy experiments. The image depicts a muon reaching the sample and undergoing precession by the action of a magnetic field. Eventually, the muon decays into a positron, which is then recorded by either the F or B detector (sourced from [Gug20]).

Muon spectroscopy experiments offer three distinct geometries for conducting measurements: transverse, longitudinal, and zero-field. Transverse geometry or muon spin rotation employs a magnetic field that is perpendicular to the spin direction of the muon, as illustrated in Fig. 2.5. Longitudinal geometry or muon spin relaxation, on the other hand, utilizes a magnetic field that is parallel to the muon's spin direction, with the magnetic field in Fig. 2.5 oriented along the y-axis. Finally, zero-field geometry, also called muon spin relaxation involves the complete absence of an applied magnetic field.

As will be seen in Chapter 3, the three geometries mentioned above were used to investigate the behavior of the muonium in the CIGS and CZTS samples.

2.4 EMU Instrument and European Commission (EC) muon beam line.

The CIGS and CZTS samples were analyzed using the EMU μSR spectrometer (Figure 2.7) at the ISIS facility at Rutheford-Appleton Laboratory in the United Kingdom.

The following briefly describes the technical characteristics of the EMU instrument and how the muon beam that reaches it is produced through the EC muon beam line (Fig. 2.6).

In the EC's muon beam line, a proton beam with an energy of 800 MeV initially hits a graphite target called the production target. As a result of this collision, pions are produced from rest on the surface of the target. The pions then decay into so-called surface muons or Arizona muons. These muons have a well-defined momentum and energy of 26.5 MeV/c and 3.8 MeV, respectively. Since the muons emerge from the production target in random directions, each magnetic quadrupole is responsible for focusing the muon beam. Both magnetic dipoles bend the muon beam (net angular deviation of 90°), thus adapting it to the geometry of the line and selecting particles with different charge and velocity values. Between these dipoles is a set of momentum slits, which can be adjusted so that only the particles with the desired momentum can pass through. However, these dipoles and slits cannot prevent muon beam contamination, mainly by positrons with the same momentum as the muon but with different velocities. To avoid such contamination, a separator is used to eliminate unwanted particles. Finally, the kickers send the beams one at a time to each instrument in the experimental area to avoid overlapping beams in a single muon instrument [Blu+22, Hil+19, Hil+22].

The muon beam can penetrate the sample to a depth of approximately 500 μm and is generated at a rate of 4 x 10^5 μ^+/s. Since the proton beam is produced through finite pulses whose full width at half maximum is 80 ns, the observable frequency in the EMU is limited to a maximum of 10 MHz.

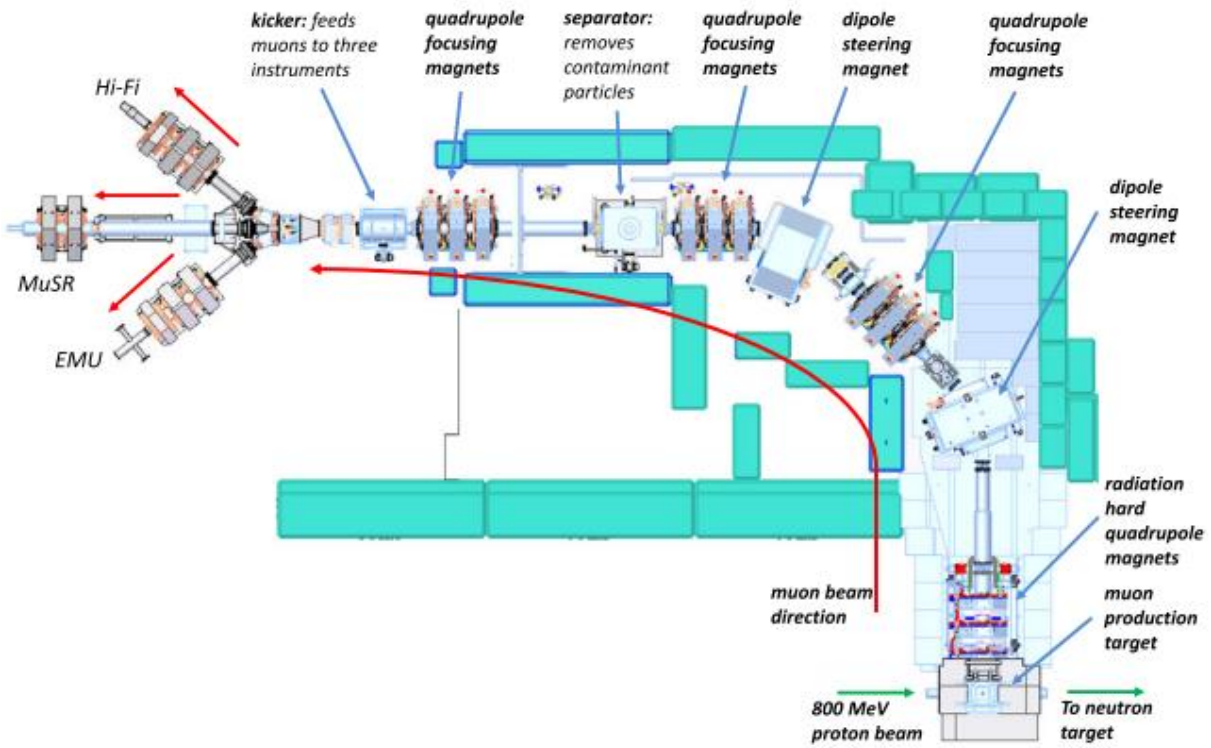

Figure 2.6: Scheme of the EC Muon beamline at ISIS. The proton beam hits the production target with an energy of 800 MeV, starting the production of the muon beam (bottom right). The devices used to guide and clean the muon beam until it reaches the experimental area (top left) are displayed. In addition to the EMU, there are two other spectrometers, the Hi-Fi and the MuSR, which share the same beam. The red arrows represent the muon beam, and the green arrows represent the proton beam (from [Hil+19]).

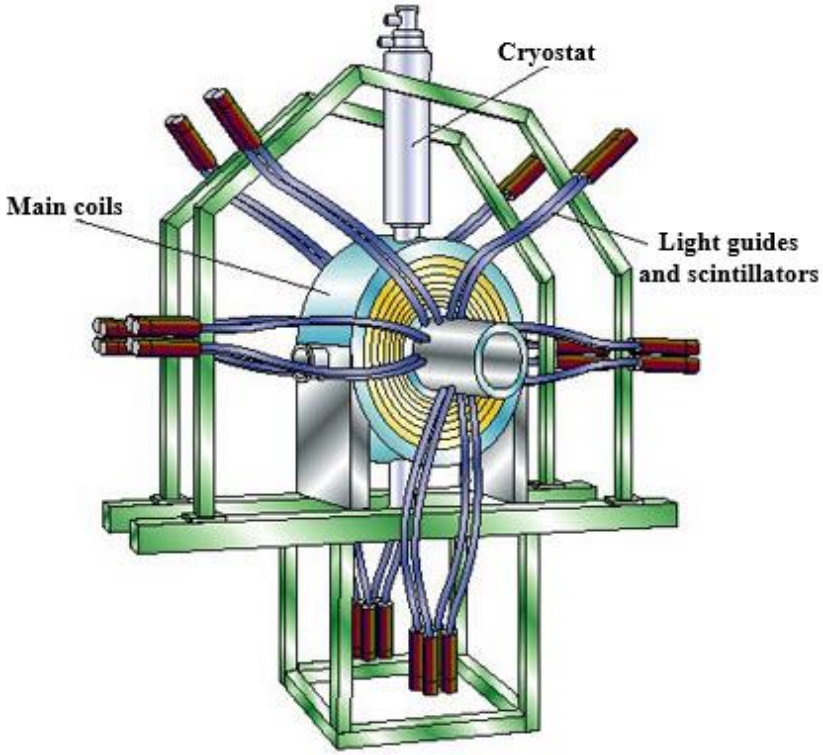

Figure 2.7: A schematic diagram of the EMU spectrometer at the Rutherford Appleton Laboratory's ISIS facility is shown, highlighting the cryostat, coils responsible for the longitudinal field, and light guides coupled to the scintillators (from [ISI]).

The EMU instrument (Fig. 2.7) is an μSR spectrometer optimized for zero field and longitudinal measurements. The positron detectors consist of 32 scintillator segments arranged in two rings of 16 detectors. The rings are arranged so that the beam coincides with the axis of cylindrical symmetry. The signal from the detectors is transferred by light guides to the photomultipliers.

Longitudinal fields of up to 4000 G can be applied via a set of Helmholtz coils. A transverse field of up to 100 G can be achieved through a set of supplementary coils. Transverse field measurements are used for calibration measurements (see Chapter 3).

Sample temperatures in the range of 350mK to 1000K can be produced using a variety of sample environment equipment. In this work, the CCR (closed cycle refrigerated) cryostat was used, which allowed the samples to be subjected to a range of temperatures from 10 to 600 K.

2.5 Muonium

Hydrogen impurities in semiconductor materials are inherent to their growth and manufacturing process. The presence of this element drastically affects the electrical and optical properties of these materials [Nic99].

When implanted in matter until its thermalization, the muon can capture an electron, thus forming the so-called muonium state, Mu = [μ+e^-], whose chemical properties resemble those of hydrogen. In this way, muonium can be considered a pseudo-light isotope of hydrogen and, therefore, simulate an impurity of hydrogen. Furthermore, such contaminants are difficult to study directly, making μSR spectroscopy an excellent choice for identifying intrinsic hydrogen-like states in semiconductors.

The following Hamiltonian describes the spin interaction between the muon's spin and the electron's spin.

$$\mathcal{H} = A\mathbf{S}_\mu \cdot \mathbf{S}_e. \tag{2.11}$$

Here $\mathbf{S}_\mu$ and $\mathbf{S}_e$ are muon's and electron's spin operators, respectively, and A = 4463 MHz [Cox09] is the value of the hyperfine coupling constant in a vacuum. The expression for the hyperfine constant is

$$A = \frac{2}{3}\hbar^2 \mu_0 g_e \mu_B g_\mu \gamma_N |\psi(0)|^2 \tag{2.12}$$

where g_e is the electron g factor, μ_B is the Bohr magneton, g_μ is the muon g factor, γ_N is the nuclear magneton, and $|\psi(0)|^2$ is the probability density for the unpaired electron ground state. The magnitude of A indicates the degree of delocalization of the unpaired electron density.

Applying an external magnetic field creates an additional interaction between muon and electron spins called the Zeeman interaction, corresponding to the splitting of energy levels in muonium (Fig. 2.7). As an effect, the Hamiltonian (Eq. 2.11) acquires two further terms, namely

$$\mathcal{H} = A\mathbf{S}_\mu \cdot \mathbf{S}_e + \boldsymbol{\mu}_e \cdot \mathbf{B} + \boldsymbol{\mu}_\mu \cdot \mathbf{S}_e \tag{2.13}$$

where $\boldsymbol{\mu}_e$ and $\boldsymbol{\mu}_\mu$ are the magnetic moment operators of the muon and the electron, respectively.

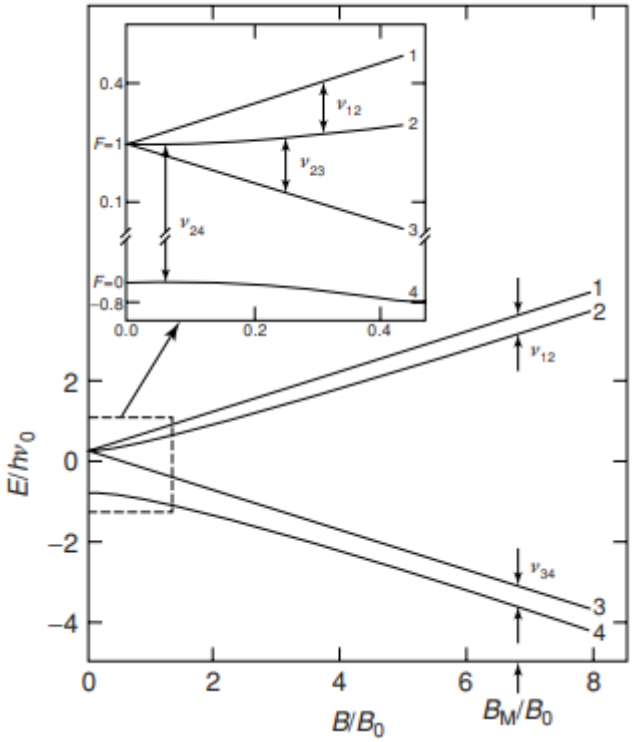

Figure 2.8: Split of the energy levels of the isotropic muonium in its ground state as a function of an applied external field. The energy is in units of $h\nu_0$ (ν_0 = 4.463.3 MHz), and the magnetic field is in units of B_0 (0.1585 T). The corresponding transition frequencies are shown for low fields (inset) and the transition frequencies for high fields (from [Kie+84]).

Semiconductors commonly have three types of muonium configurations: normal, anomalous, and ionized. Normal or isotropic muonium, Mu, has a spherically symmetric electron cloud. When interacting with the medium, its hyperfine constant is typically less than or slightly higher than the vacuum's. This muonium configuration typically corresponds to a nearly atomic-like state, usually at an interstitial location. Another variety, formerly known anomalous muonium, Mu^*, exhibits a distortion in its electronic cloud, leading to an anisotropic hyperfine interaction depending on the crystal orientation. The magnitude of this interaction is generally much smaller than that of isotropic muonium. This variety corresponds to a muonium atom that reacted with the lattice, forming a bond with an atom of the solid, either in a bond center position (as occurs typically in the elemental and III-V semiconductors) or in an anti-bonding position (as occurs typically in II-VI semiconductors and oxides). Both Mu and Mu^* form paramagnetic (neutral) muon states. Ionized muonium, Mu^+, i.e., the muon itself, is a diamagnetic (charged) muon state. One second diamagnetic form occurs when the muon captures two electrons, generating a negatively charged muonium state Mu^-. However, such a configuration is exceptionally improbable, except for a highly doped n-type material above the ionization temperature [Hit99]. This configuration also appears in an interstitial site.

We note that the typical values of the hyperfine interaction lead to muon spin precession frequencies much higher than the maximum detectable frequency at ISIS (c. 14 MHz). The presence of muonium can therefore be usually inferred only in an indirect way, through the disappearance of the muon asymmetry signal (known as the missing fraction). The hyperfine interaction of muonium can nevertheless be determined in such circumstances by applying a strong magnetic field in the direction of the initial muon spin. The competition of the hyperfine interaction and the Zeeman interaction leads to a repolarization of the muon spin, with the following dependence:

$$P = \frac{1}{2} + \frac{x^2}{2(1+x^2)}. \tag{2.14}$$

Here, $x = B/B_0$, where $B_0 = 0.15853$ T corresponds to the hyperfine magnetic field of the muonium when it is in a vacuum, and B corresponds to an applied external magnetic field parallel to the initial muon spin direction. P is the muon spin polarization.

2.6 μSR in chalcopyrite semiconductors: state-of-the-art

Muon spin spectroscopy has already proved to be an invaluable technique in modelling the behavior and configurations of hydrogen in chalcopyrite materials: the Coimbra μSR group has characterized the donor configuration in $CuInSe_2$, by both determining its bonded position to a Se anion, at an antibonding site [Gil+99], and proposing the corresponding donor level [Vil+03a]. The muon diffusion has also been thoroughly investigated in CuInSe2 and other related chalcopyrite semiconductors [Gil+99, Vil+03b], and the subsequent trapping at native defects (presumably Cu vacancies) has been observed [Vil+03b]. Hints of the presence of a deep acceptor-like configuration were also observed in chalcopyrite [Gil+99]. In structurally related II-VI semiconductors, these acceptor-like configurations have been fully investigated [Vil+05], leading to the corresponding acceptor levels [Vil+08]. In this dissertation we therefore intend to complete the characterization of the hydrogen impurity in CZTS and CIGS, by using the positive muons as an analogue [Vil+15]. Muon spin spectroscopy using slow muons has also been used to extract relevant microscopic information about semiconductor surfaces and interfaces, in particular the width of the defect layer in CdS/CIGS [Alb+18], where hydrogen is likely to play a determinant role. Recent data in bulk and thin-film CZTS and CIGS [Alb+18, Alb14] revealed that the μSR signal is basically diamagnetic, with 20% missing fraction (likely corresponding to a deep muonium state with a high hyperfine interaction). The diamagnetic

fraction can be separated in two components with different relaxations, the component with higher relaxation likely corresponding to a transition muonium state with a small hyperfine interaction (a couple of MHz) [Vil+17, Vil+18]. The diamagnetic signal, corresponding to muons stopping in the positively charged configuration, can be characterized with utmost precision at ISIS. In particular, measurements in zero field allow to follow with great precision the relaxation of the diamagnetic component. This relaxation is seen to decrease with temperature as the muons start diffusing through the sample (around 200 K). As the muons diffuse through the sample, the probability of capture by a defect increases and this is expected to impact on the relaxation, usually through "trapping peaks" [Vil+03a]. The missing fraction in the PSI experiments likely corresponds to muons stopping as neutral muonium, which are expected to be accessible at ISIS by recovering the muon spin polarization with increasing longitudinal fields. The corresponding repolarization curve will allow to extract the hyperfine interaction, as well as details of the spin dynamics.

Chapter 3: Results

3.1 Experimental Details

We will now present the new experimental muon-spin spectroscopy measurements on bulk CIGS and bulk CZTS, undertaken at the ISIS Muon and Neutron Facility in Chilton, UK, by the Coimbra μSR team in March 2020. Polycrystalline samples were obtained from the Laboratory of Photovoltaic Materials, Department of Materials and Environmental Technology, Tallinn University of Technology, Tallinn, Estonia, which were grown by the team of Dr. Marit Kauk-Kuusik. The Ga content of the CIGS sample corresponds to a value of around 20%, typical of practical solar cells. Precisely, $Cu(In_{0.79}Ga_{0.21})_{1.09}Se_{2.1}$ and CZTS polycrystalline samples were measured in the following experimental conditions, which we will present and analyze in detail in the course of this chapter:

- Transverse field measurements for samples at temperature T = 50 K
- Longitudinal field measurements for sample temperatures corresponding to T = 10 K, 100 K, 175 K and 400 K.
- Transverse field (at low field) and zero field measurements as a function of temperature.

In the course of this chapter, we will present the experimental results and data analyses of the above mentioned measurements. We will leave the discussion for Chapter 4.
In order to calibrate the maximum instrumental asymmetry, measurements in a silver sample were performed as well. All the measurements were done in a sample holder appropriate for holding powder samples. However, the muon beam spot being rather large, a non-negligible fraction of muons stops in the sample holder. In order to calibrate the asymmetry signal of the sample holder, a hematite (Fe_2O_3) sample was used since the muon asymmetry is zero in this magnetic material. The extremely delicate calibration procedure will also be thoroughly discussed in the course of this chapter.

3.2 Calibration measurements

3.2.1 Calibration of the signal due to the sample holder using hematite

Measurements of the sample holder with the (dummy) hematite sample were performed at room temperature (RT), in transverse geometry with fields from 0 G to 100 G. A typical signal is shown in Fig. 3.1:

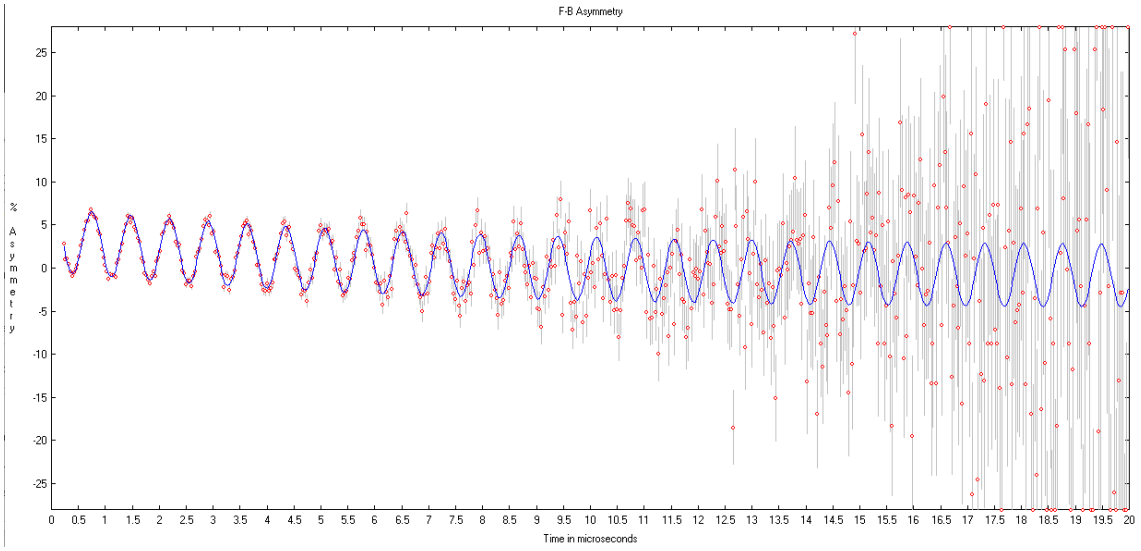

Figure 3.1: Typical signal coming from the sample holder when using a dummy hematite sample

This signal is rather complex to describe, with an oscillation superimposed to a relaxing signal. Our best description is by a three-component fit as follows:

$$A(t) = A_1\cos(2\pi f_1 t + \varphi_1) + A_2\exp(-\lambda_2 t) + A_3 \qquad (3.1)$$

As shown in the Figs. 3.2, 3.3, 3.4, 3.5, 3.6 and, 3.7 below, the best fits to the transverse field dependence were obtained by fixing the instrumental alpha parameter (to $\alpha = 1.19$)

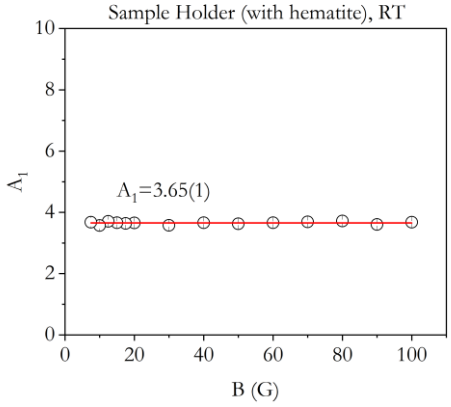

Figure 3.2: Amplitude component A_1 as a function of the transverse magnetic field B.

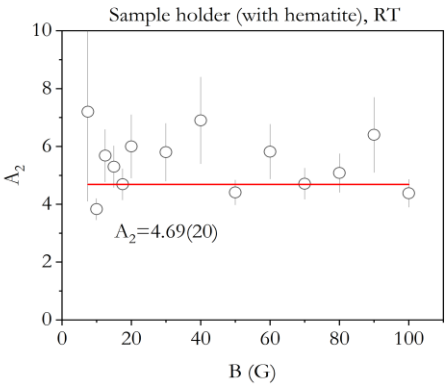

Figure 3.3: Amplitude component A_2 as a function of the transverse magnetic field B

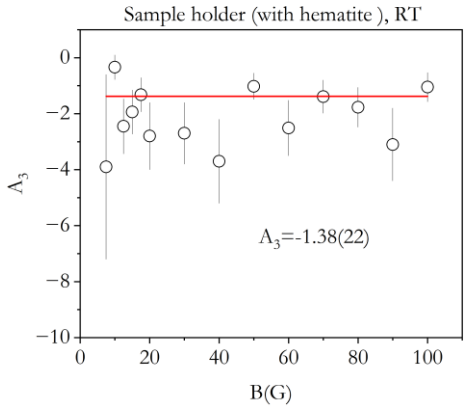

Figure 3.4: Amplitude component A_3 as a function of the transverse magnetic field B.

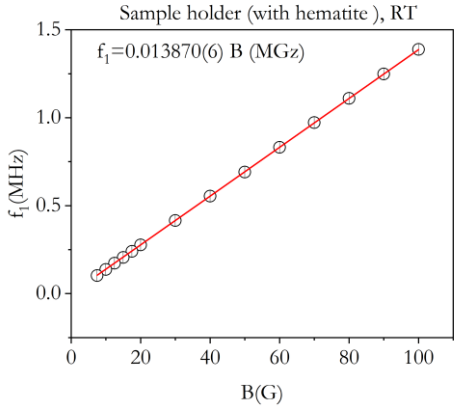

Figure 3.5: Linear dependence of frequency f_1 on transverse magnetic field B.

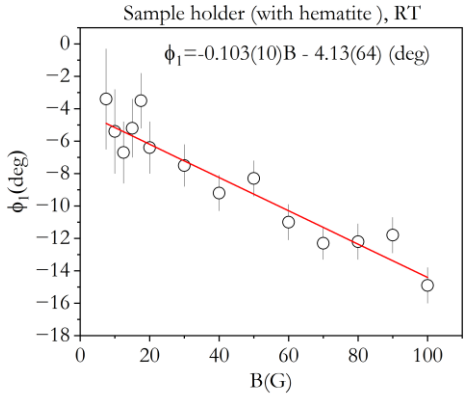

Figure 3.6: Phase ϕ_1 as a function of the transverse magnetic field B.

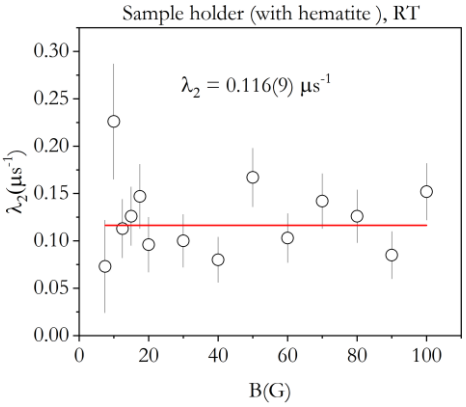

Figure 3.7: Relaxation λ_2 as a function of the transverse magnetic field B.

The fits in the figures above show that the amplitudes and relaxation are approximately the same for all fields:

$$A_1 = 3.65(1),\ A_2 = 4.69(20),\ A_3 = -1.38(22),\ \lambda_2 = 0.116(9)\ \mu s^{-1}$$

The phase, as expected, varies in an approximately linear way with the applied magnetic field B:

$$\varphi_1 = -0.103(10)\mathrm{B} - 4.13(64) \qquad (3.2)$$

The precession frequency can be fitted to a linear relation, indicating that the nominal field B is slightly higher than the true field as measured by the frequency.

$$f_1 = 0.013870(6)\mathrm{B} \qquad (3.3)$$

3.2.2 Calibration of the maximum asymmetry using silver

In order to obtain the value of the maximum asymmetry for the instrument, we measured a silver sample more or less with the sample size. For the analysis of this data, we assume that we also have a contribution from muons stopping in the sample holder (see Eq. 3.1). We have modelled this contribution using the same shape and parameters as described above, while adjusting the alpha parameter (in case a fixed alpha is used, the baseline variation is included in parameter A_3). We have therefore fitted the data of the Ag sample on the sample holder with the function

$$A(t) = A_{Ag}\cos(2\pi f_{Ag}t + \varphi_{Ag}) + A_1\cos(2\pi f_1 t + \varphi_1) + A_2\exp(-\lambda_2 t) + A_3 \qquad (3.4)$$

where A_1, A_2, A_3, f_1, φ_1 and λ_2 were fixed to the values found for the sample holder. With respect to the precession parameters f_1, φ_1, f_{Ag} and φ_{Ag}, we have compared the data at TF = 100 G and verified that

f_{Ag} = 1.38747(19) MHz and f_1 = 1.38794(91) MHz

φ_{Ag} = − 7.3(2) ° and φ_1= − 14.4(11) °

This indicates us that it is appropriate to fix $f_{Ag} = f_1$ and leave it as a single free parameter. However, the same cannot be done with the phases, so the best approach seems to be fixing φ_1 to the value obtained for the sample holder at a given field and leave φ_{Ag} as a free parameter. Figs. 3.8, 3.9 and 3.10 below show the results for A_{Ag}, f_{Ag}, φ_{Ag} to be used as calibration when comparing with the sample results.

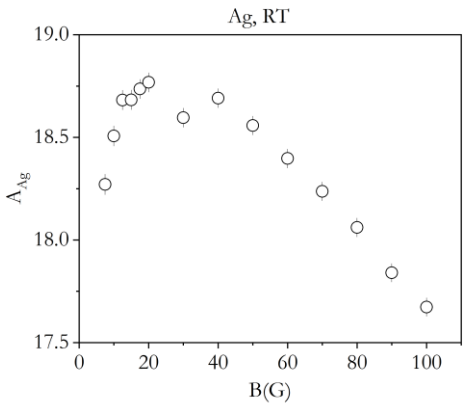

Figure 3.8: Amplitude component A_{Ag} as a function of the transverse magnetic field B

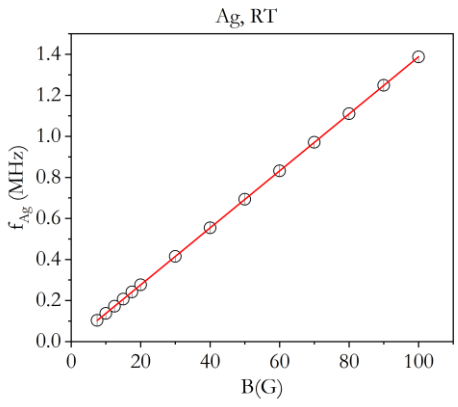

Figure 3.9: Linear dependence of frequency f_{Ag} on transverse magnetic field B.

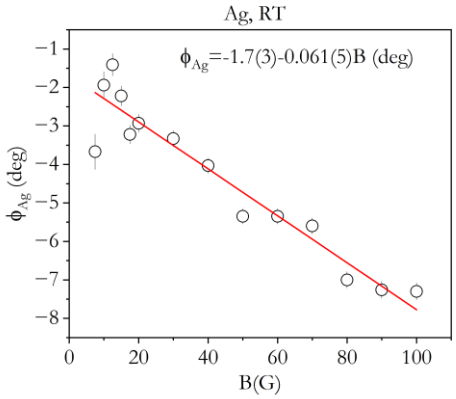

Figure 3.10: Phase ϕ_{Ag} as a function of the transverse magnetic field B.

3.2.3 Correcting the size of the sample at TF = 5 G

Later on, we verified that the maximum asymmetry of the CIGS or CZTS samples is slightly different from that obtained above for Ag, due to the different sizes of the samples. In fact, when normalizing using the Ag values, we obtained values for the diamagnetic fraction at T = 600 K, in CIGS and in CZTS, that were above 100 %. This allowed us to correct the maximum asymmetry in both samples, by using the corresponding values at T = 600 K and TF = 5 G:

- For CIGS: A = 18.512(48)
- For CZTS: A = 18.714(47)

3.2.4 Correcting the size of the sample at other fields

The asymmetry for Ag at TF = 5 G is A = 17.907(34). When comparing to the values obtained above for the maximum asymmetry in CIGS and CZTS we verify that:

- For CIGS the maximum asymmetry is a factor 18.512/17.907 = 1.0338 larger;
- For CZTS the maximum asymmetry is a factor 18.714/17.907 = 1.0451 larger;

We therefore assume that these ratios correspond to the ratios between the corresponding sizes of the samples, so that, for any field B:

- For CIGS the maximum asymmetry is 1.0338*asym (Ag, B);
- For CZTS the maximum asymmetry 1.0451*asym (Ag, B).

3.3 TF dependence at T = 50 K

We begin the presentation and analysis of the experimental data with the field dependent study in transverse geometry at T = 50 K. Fig 3.11 below shows an example time spectrum at B = 15 G in CIGS. A clear relaxing oscillation is seen. As we shall see below when presenting the zero-field data, this oscillation may be compound of more than one component precessing at the muon diamagnetic frequency, with different relaxations. An important question these measurements at T = 50 K tried to answer is the possibility of distinguishing a fast and a slow relaxing component. We will begin the analysis of this data by discussing the possibility of separating these two components also in the transverse field data. We will take CIGS as an example, but the conclusions are applicable to both CIGS and CZTS.

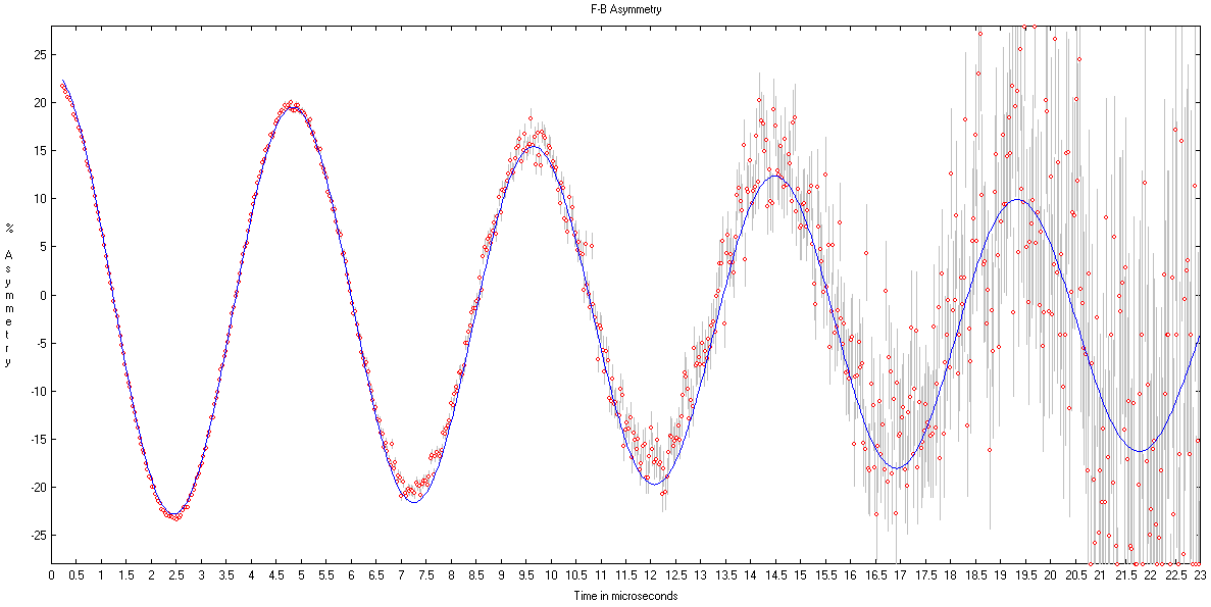

Figure 3.11: Time spectrum at B = 15 G with a relaxing oscillation

3.3.1 Is it possible to separate fast from slow components?

As mentioned above, in the data there is always a substantial background signal from the sample holder, which was calibrated using a dummy hematite sample (Section 3.2.1). This signal has a complex description with three components: an oscillating component at the Larmor frequency, a Lorentzian relaxing component, and a negative baseline (see Eq. 3.1). This signal from the sample holder was fixed in the analysis of the CIGS or CZTS samples, but the baseline was allowed to vary in order to accommodate the change in alpha when the CIGS/CZTS sample is in.

3.3.2 Trying to describe a slow component at longer times (t>c.10-12μs)

A common way to try to separate two relaxing components occurs when one of component relax sufficiently fast not be present at longer times. Fig. 3.12 shows a fit and fit results of a

single Gaussian damped component (plus background) in the time region 12 – 23 μs. We not that:

a) The precession frequency is the same as that of the background (within the error), but not the phase;
b) The spectrum looks slightly offset from asymmetry = 0, but this is a background effect present in the dummy sample holder measurement.

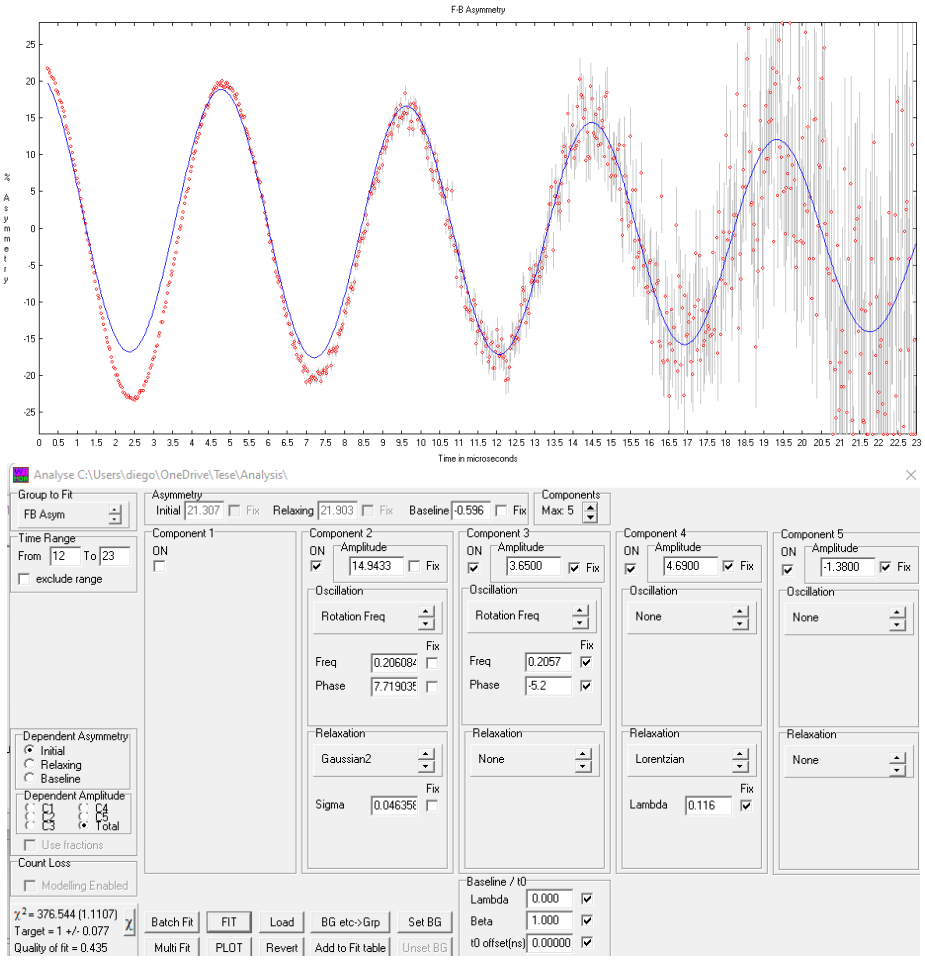

Figure 3.12: Top: fit of a single Gaussian damped component with background. **Bottom**: fit results of a single Gaussian damped component in the region 12 – 23 μs^{-1}.

Fitted parameter values:

a-baseline -0.60 (+/-0.28)
C2 Rel Ampl 14.9 (+/-1.4)
C2 Frequency 0.2061 (+/-0.0028)
C2 Phase 7.7 (+/-14)
C2 Sigma 0.0464 (+/-0.0097)
Chi squared is 376.544 (1.11075 per dof)
Chi squared target (1 +/- 0.077) Quality of fit = 0.435

3.3.3. Trying to describe a fast component at shorter times (t<c.10-12μs)

Figures 3.13, 3.14, and 3.15 below show several fits and fit results obtained by fixing the parameters of the previous fit (Fig. 3.12) and adding a second relaxing component to describe the behavior at shorter times. Several functional relaxations were tried for this additional component.

I) Gaussian relaxation

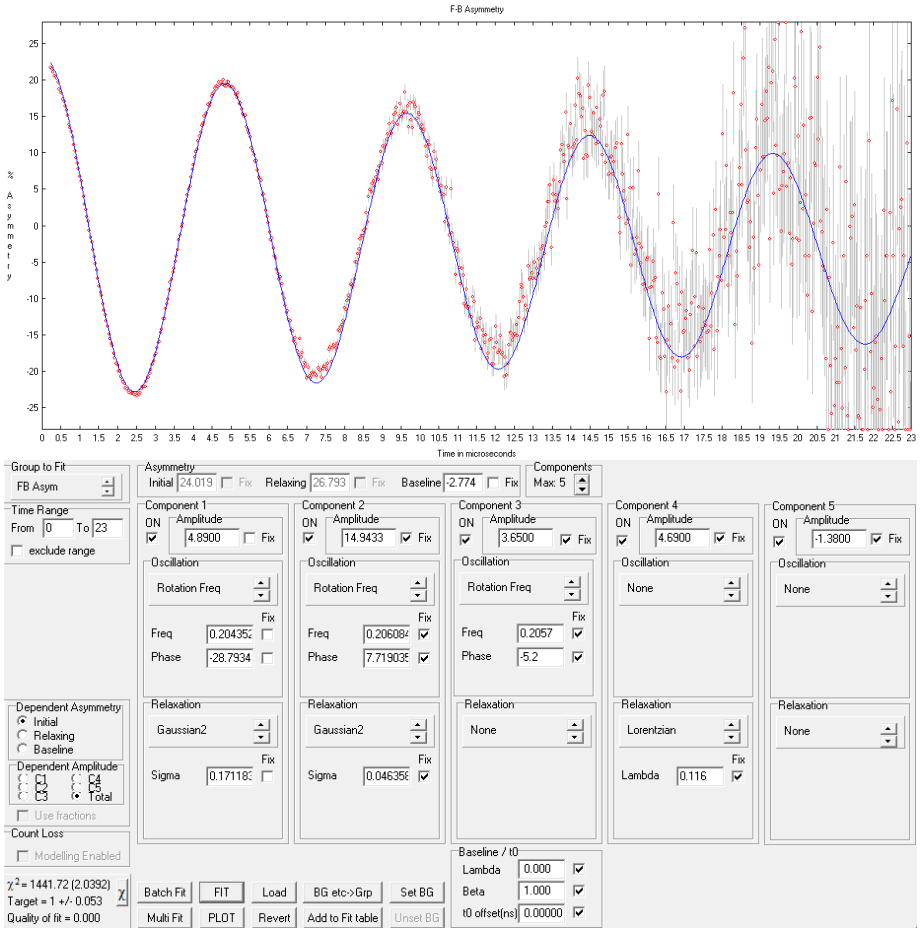

Figure 3.13: Top: fit obtained by adding a second Gaussian relaxing component. **Bottom**: fit results with adding the second Gaussian component in the region 0 – 23 μs^{-1}.

Fitted parameter values:

a-baseline -2.774 (+/-0.019)
C1 Rel Ampl 4.890 (+/-0.026)
C1 Frequency 0.20435 (+/-0.00070)
C1 Phase -28.79 (+/-0.69)
C1 Sigma 0.1712 (+/-0.0031)
Chi squared is 1441.72 (2.0392 per dof)
Chi squared target (1 +/- 0.053) Quality of fit = 0.0

II) Lorentzian relaxation

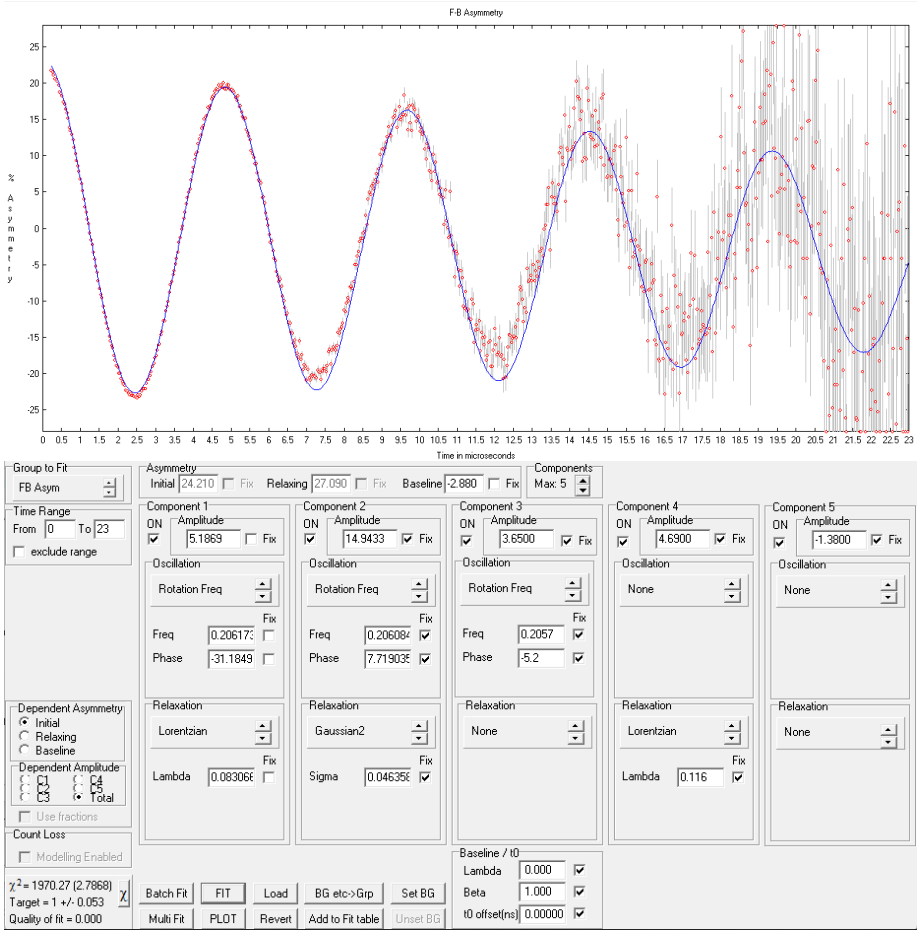

Figure 3.14: Top: fit obtained by adding a Lorentzian relaxing component. **Bottom**: fit results with adding the Lorentzian relaxing component in the region 0 – 23 μs^{-1}.

Fitted parameter values:

a-baseline -2.880 (+/-0.020)
C1 Rel Ampl 5.187 (+/-0.036)
C1 Frequency 0.20617 (+/-0.00059)
C1 Phase -31.18 (+/-0.64)
C1 Lambda 0.0831 (+/-0.0030)
Chi squared is 1970.27 (2.78681 per dof)
Chi squared target (1 +/- 0.053) Quality of fit = 0.000

III) Stretched – exponential relaxation

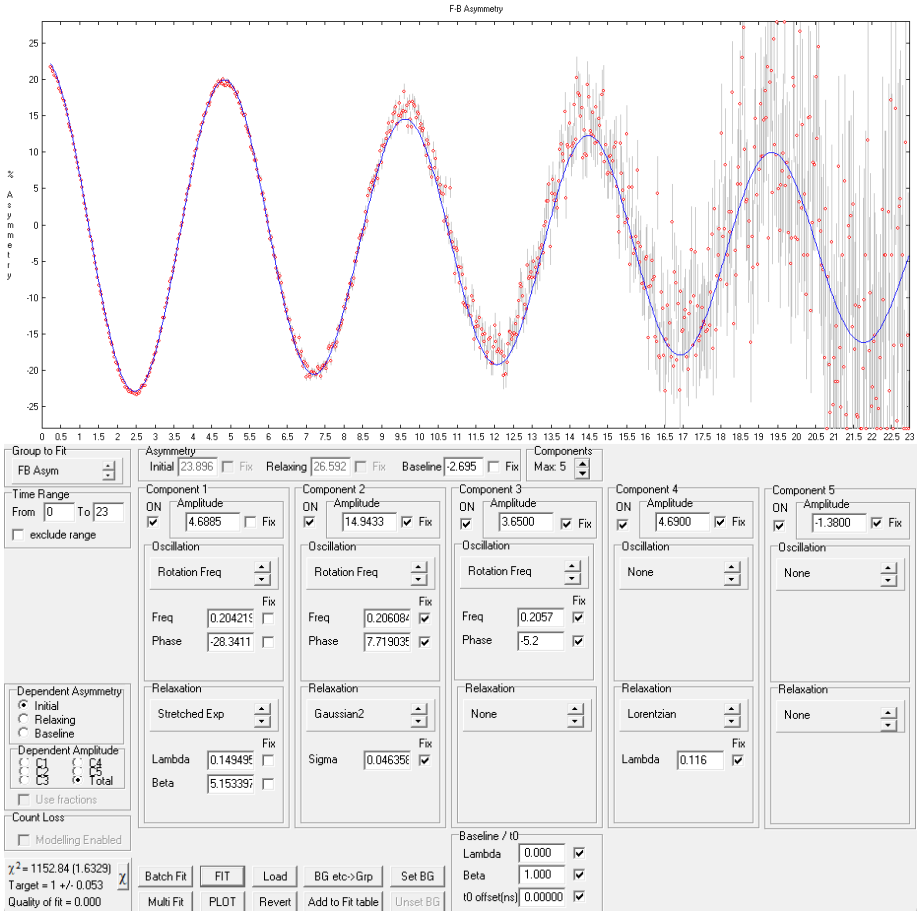

Figure 3.15: Top: fit obtained by adding a stretched relaxing component. **Bottom**: fit results with adding the stretched relaxing component in the region 0 – 23 μs^{-1}.

Fitted parameter values:

a-baseline -2.695 (+/-0.020)
C1 Rel Ampl 4.688 (+/-0.024)
C1 Frequency 0.20422 (+/-0.00079)
C1 Phase -28.34 (+/-0.77)
C1 Lambda 0.1495 (+/-0.0017)
C1 Beta 5.15 (+/-0.29)
Chi squared is 1152.84 (1.63292 per dof)
Chi squared target (1 +/- 0.053) Quality of fit = 0.000

The fits above (Figs. 3.13, 3.14, and 3.15) clearly show that a separation of the two components is extremely difficult. In particular, the precession frequency of the component at shorter times is seen both at higher and lower values than the precession frequency of the component at larger times, depending on the functional form of the relaxation.

We have thus decided to fit the sample signal with a single relaxing component. The figures 3.16 and 3.17 below show a tentative fit with a stretched exponential relaxation: the fit converges to $\beta = 2$; we have thus settled in a gaussian relaxing form.

IV) Fit single component (stretched exponential relaxation)

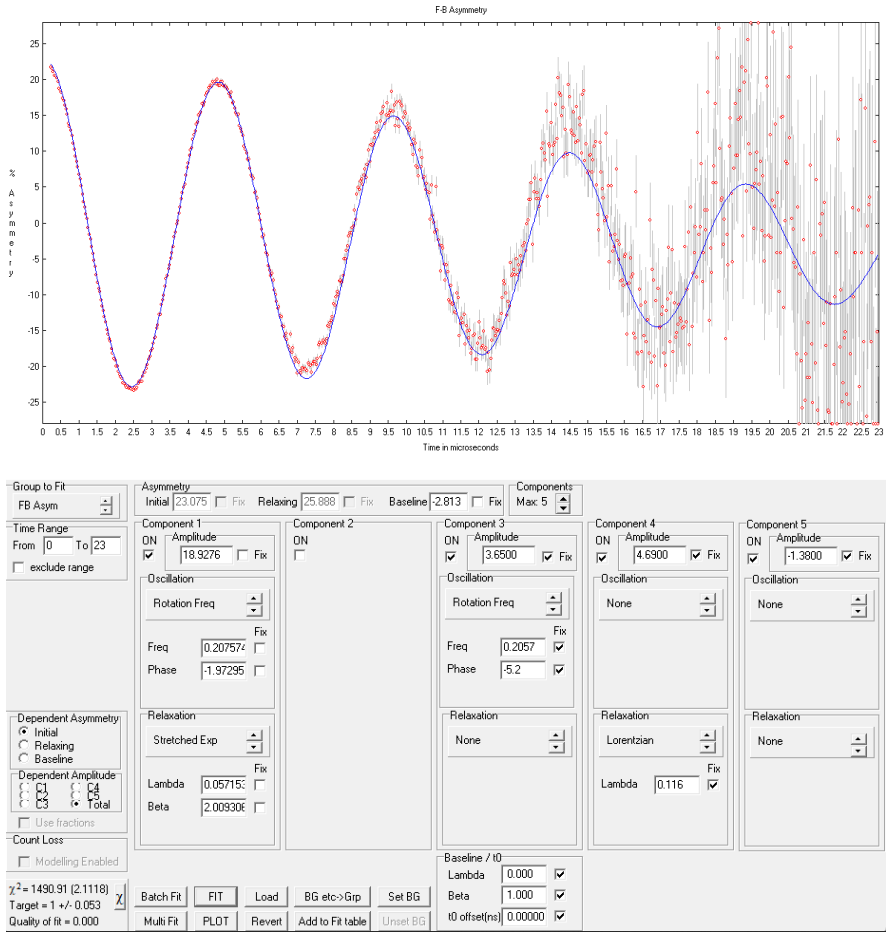

Figure 3.16: Top: fit obtained using a stretched relaxing component. **Bottom**: fit results with $\beta = 2$ in the region 0 – 23 μs^{-1}.

Fitted parameter values:

a-baseline -2.813 (+/-0.019)
C1 Rel Ampl 18.928(+/-0.034)
C1 Frequency 0.20757 (+/-0.00011)
C1 Phase -1.97 (+/-0.13)
C1 Lambda 0.0572 (+/-0.0012)
C1 Beta 2.009 (+/-0.059)
Chi squared is 1490.91 (2.11177 per dof)
Chi squared target (1 +/- 0.053) Quality of fit = 0.000

V) Fit single component (gaussian relaxation)

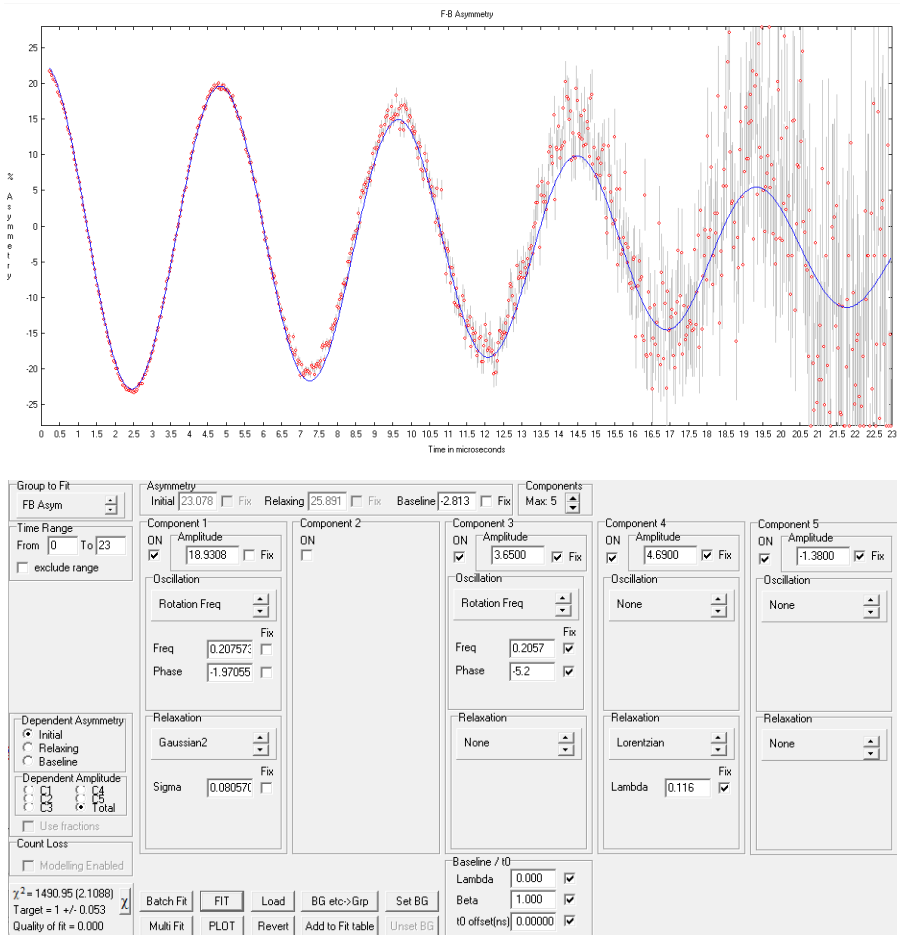

Figure 3. 17: Top: fit obtained using a Gaussian relaxing component. **Bottom**: fit results in the region $0 - 23\ \mu s^{-1}$.

Fitted parameter values:

a-baseline -2.813 (+/-0.019)
C1 Rel Ampl 18.931(+/-0.026)
C1 Frequency 0.20757 (+/-0.00011)
C1 Phase -1.97 (+/-0.13)
C1 Sigma 0.08057(+/-0.00089)
Chi squared is 1490.95 (2.10884 per dof)
Chi squared target (1 +/- 0.053) Quality of fit = 0.000

3.3.4. CIGS: one component fits (Gaussian relaxation)

We have therefore fitted the CIGS data with a single component with gaussian relaxation, modeling the signal of the sample holder as before (complex signal with three components: oscillation plus relaxation plus baseline). The total fitting function was therefore

$$A(t) = A_{sample} + A_{sample\ holder} + A_{baseline} \tag{3.5}$$

$$A_{sample} = A_{CIGS} \exp\left(-\frac{1}{2}\sigma^2 t^2\right) \cos(2\pi f_{CIGS} t + \varphi_{CIGS}) \tag{3.6}$$

$$A_{sample\ holder} = A_1 \cos(2\pi f_1 t + \varphi_1) + A_2 \exp(-\lambda_2 t) + A_3 \tag{3.7}$$

where the parameters of the sample holder were fixed and the additional parameter A_3 baseline is meant for small adjustments of the baseline due to the field variation. The results are shown in Figs. 3.18, 3.19, 3.20, 3.21, 3.22, 3.23, 3.24, 3.25 and, 3.26 below. The fraction was calculated using the calibration for the maximum asymmetry performed as explained in Section 3.2.4.

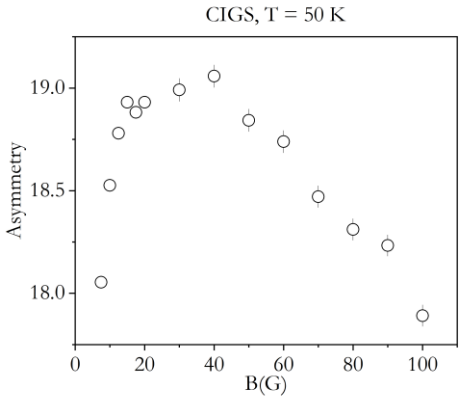

Figure 3.18: The maximum asymmetry as a function of the applied magnetic field. The graph shows that the maximum asymmetry is approximately constant with small variations that are observed in Ag as well.

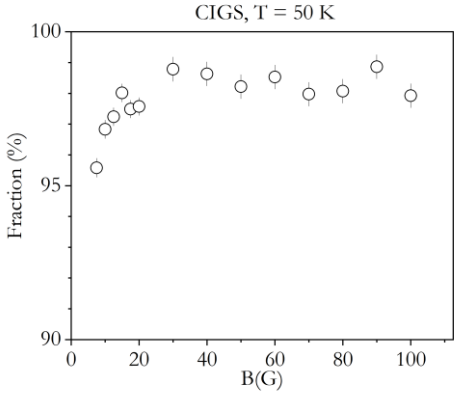

Figure 3.19: Field dependence of the diamagnetic fraction, after comparing the sample asymmetry with that of Ag. The error bars are the simple statistical ones obtained from straight error propagation. The data suggest a slight reduction of the fraction at lower fields, consistent with the presence of a small (nuclear?) hyperfine interaction.

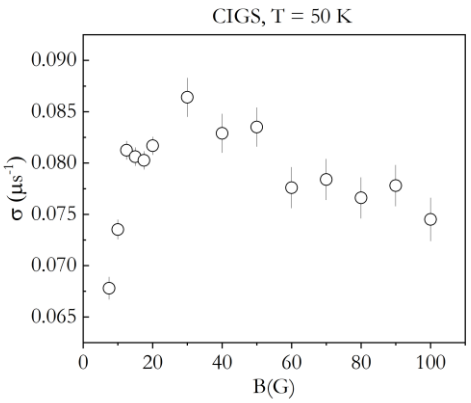

Figure 3.20: Field dependence of the muon spin relaxation rate σ.

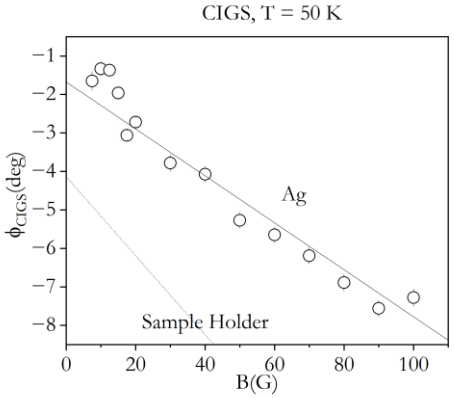

Figure 3.21: Field dependence of the muon phase. The figure also shows the field dependence of the muon phase for Ag and sample holder.

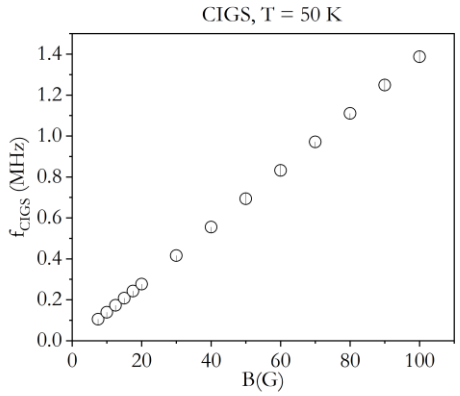

Figure 3.22: Field dependence of the muon frequency

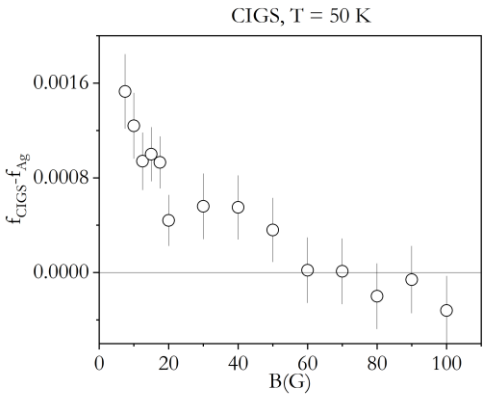

Figure 3.23: Field dependence of the difference between the frequency of the CIGS and silver. A clear frequency shift is observed below 60 G. This is consistent with a hyperfine interaction around 1 MHz.
[Note: during the measurements, the field at the nearby HIFI instrument was always at B = 2T; the field at the MUSR instrument changed from B = 550G to B = 75G in the course of the 15G run.]

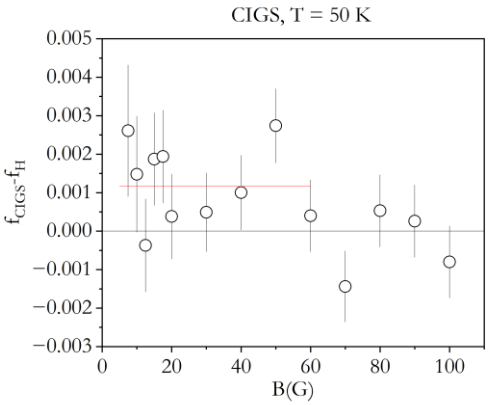

Figure 3.24: Field dependence of the difference between the frequency of the CIGS and hematite. Although the error bars are very large, a linear fit up to 60 G clearly shows an average offset of 0.0012(3), consistent with the much more precise value shown in figure 3.23.

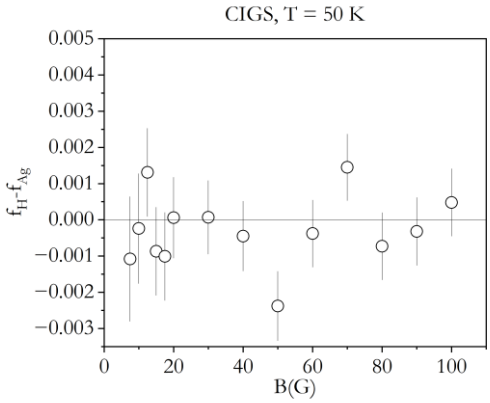

Figure 3.25: Field dependence of the difference between the frequency of the hematite and silver. The frequencies are the same within the error bars, even when considering the overall average value across all fields.

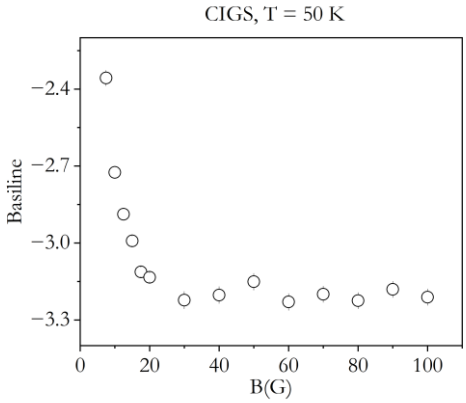

Figure 3.26: Baseline asymmetry as a function of the applied magnetic field. The graph shows that between 0 and 20 G baseline drops rapidly due to changes in positrons trajectories. However, the baseline stabilizes from 20 G to 100 G.

3.3.5 CZTS: one component fits (Gaussian relaxation)

We have also fitted the CZTS data with a single component with gaussian relaxation, modeling the signal of the sample holder as before (complex signal with three components: oscillation plus relaxation plus baseline). The total fitting function was therefore

$$A(t) = A_{sample} + A_{sample\ holder} + A_{baseline} \tag{3.8}$$

$$A_{sample} = A_{CZTS} \exp\left(-\frac{1}{2}\sigma^2 t^2\right) \cos(2\pi f_{CZTS} t + \varphi_{CZTS}) \tag{3.9}$$

$$A_{sample\ holder} = A_1 \cos(2\pi f_1 t + \varphi_1) + A_2 \exp(-\lambda_2 t) + A_3 \tag{3.10}$$

where the parameters of the sample holder were fixed and the additional parameter A_3 baseline is meant for small adjustments of the baseline due to the field variation. The results are shown in Figs. 3.27, 3.28, 3.29, 3.30, 3.31, 3.32, 3.33, 3.34 and 3.35 below.

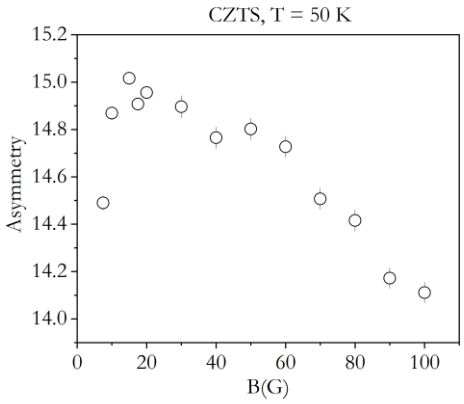

Figure 3.27: The maximum asymmetry as a function of the applied magnetic field. The graph shows that the maximum asymmetry is approximately constant with small variations that are observed in Ag as well.

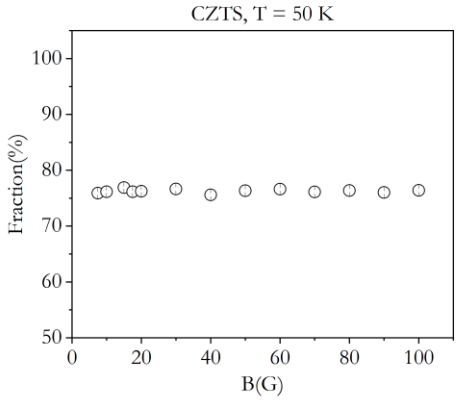

Figure 3.28: Field dependence of the diamagnetic fraction, after comparing the sample asymmetry with that of Ag. The error bars are the simple statistical ones obtained from straight error propagation.

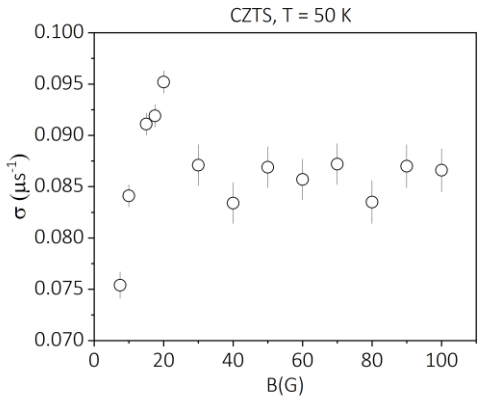

Figure 3.29: Field dependence of the muon spin relaxation rate σ.

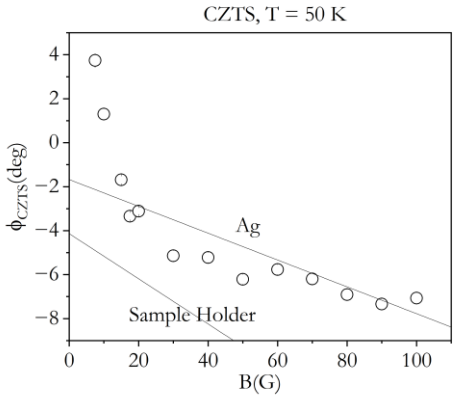

Figure 3.30: Field dependence of the muon phase. The figure also shows the field dependence of the muon phase for Ag and sample holder.

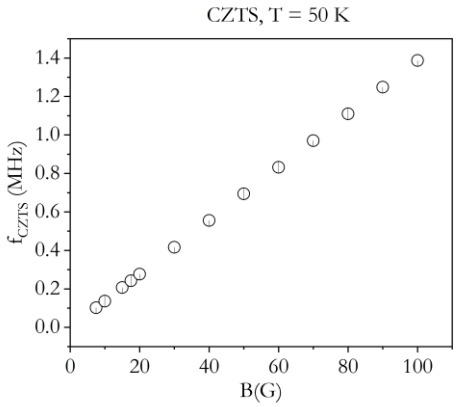

Figure 3.31: Field dependence of the muon frequency

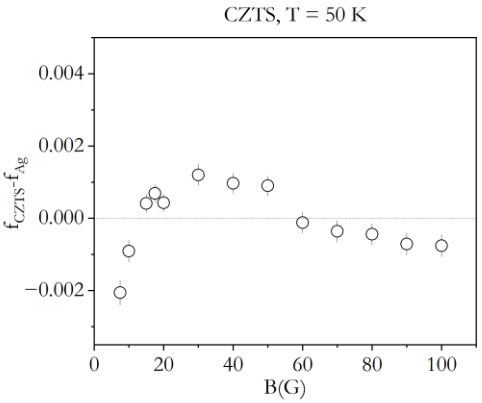

Figure 3.32: Field dependence of the difference between the frequency of the CZTS and silver. A possible frequency shift is observed below 60 G. This is consistent with a hyperfine interaction around 1 MHz.

[Note: during the measurements, the field at the nearby MUSR instrument was always at B = 0G; the field at the nearby HIFI instrument increased from B = 3.25T at the 5G run to B = 3.5T at 20G run and then decreased to B = 0T from the 20 G run up to the 100G run.]

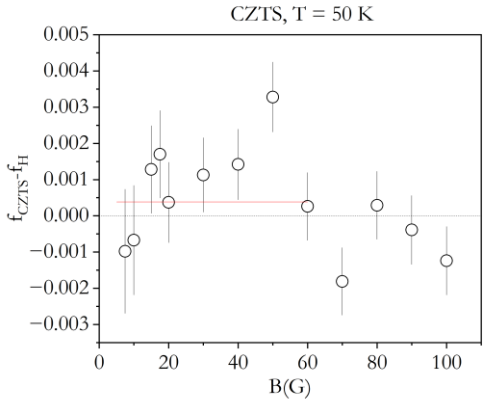

Figure 3.33: Field dependence of the difference between the frequency of the CZTS and hematite. A possible frequency shift is present for B < 60 G.

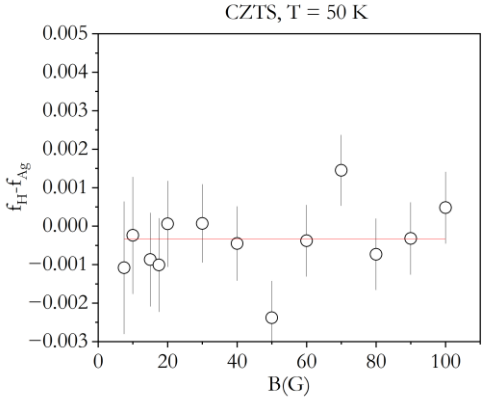

Figure 3.34: Field dependence of the difference between the frequency of the hematite and silver. This repetition of Fig. 3.25 is shown for an easier comparison with Fig. 3.33.

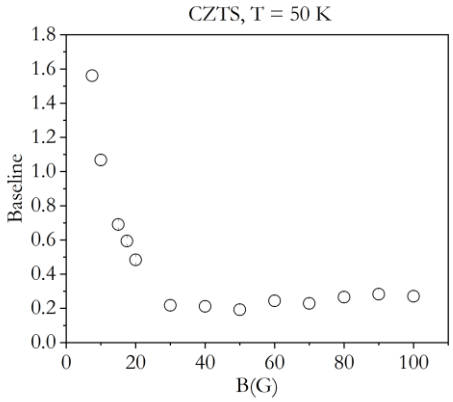

Figure 3.35: Baseline asymmetry as a function of the applied magnetic field. The graph shows that between 0 and 30 G baseline drops rapidly due to changes in positrons trajectories. However, the baseline stabilizes from 20 G to 100 G.

3.5 Measurements in longitudinal field

We now present the results of the experimental measurements in longitudinal field, aimed at characterizing possible deep muonium states. We begin, as before, with the a discussion of the calibration and then present the results on CIGS, followed by those on CZTS.

3.5.1 Characterization of sample holder and silver sample.

For the longitudinal field measurements, we only have a calibration with silver. However, these measurements allow to separate the Ag component from that of the sample holder, due to the different relaxation. The alpha parameter was determined (and fixed) from a TF = 20 G measurements: $\alpha = 1.02348(75)$. A data bunching of 2 was adopted; fits were done up to 20 μs; detector background was automatically fitted.

In order to separate the Ag and the sample holder components in the LF calibration measurements, we fitted the data with two relaxing components:

- We tried a small gaussian relaxation for Ag and could not find any relaxation even at the lowest field (LF = 2 G); we have thus fixed it to zero;
- For the relaxing component arising from muons stopping in the sample holder, we tried both Lorentzian and gaussian shape: gaussian seems to provide a more adequate description ($\sigma = 0.39(16)\ \mu s^{-1}$ at LF = 2 G)

The fit results are shown in Figs. 3.36 and 3.37 (for the asymmetries and relaxation, respectively). The parameters of the relaxing component associated to the sample holder are reasonably constant with field and were fixed to the average value for subsequent fits.

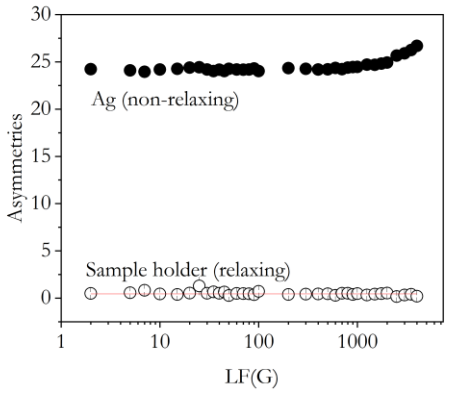

Figure 3.36: Asymmetry of the non-relaxing and relaxing components (associated to silver and to the sample holder, respectively) in the longitudinal field calibration measurements. The relaxing component is reasonably constant (A = 0.43(2)).

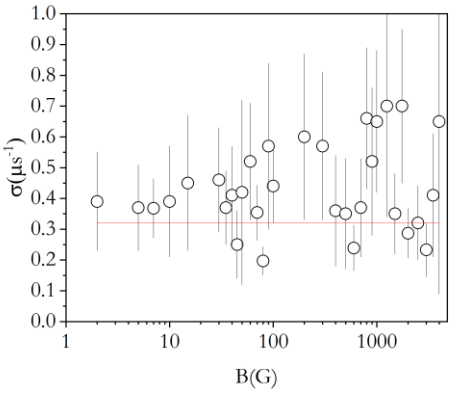

Figure 3.37: Gaussian relaxation of the relaxing component (associated to the sample holder) in the longitudinal field calibration measurements. The relaxation is reasonably constant ($\sigma = 0.32(2)\ \mu s^{-1}$).

3.6 CIGS repolarization at T =10K

For the CIGS sample, a longitudinal-field dependence (repolarization) was performed at the lowest temperature only (T = 10 K). For the analysis of the data, a small relaxing component corresponding to the muons stopping in the sample holder was fixed as described above (Section 3.5.1). The remaining data can only be fitted to a single relaxing component for LF>c.25 G; for LF <c.25 G, the sample data can be described with a constant component plus a gaussian relaxing component (and a third fixed component due to the sample holder).

3.6.1 About the shape of the relaxing component

We tried both Lorentzian and Gaussian shape for the relaxing component (Figs. 3.38 and 3.39 below). The shape is clearly closer to Gaussian.

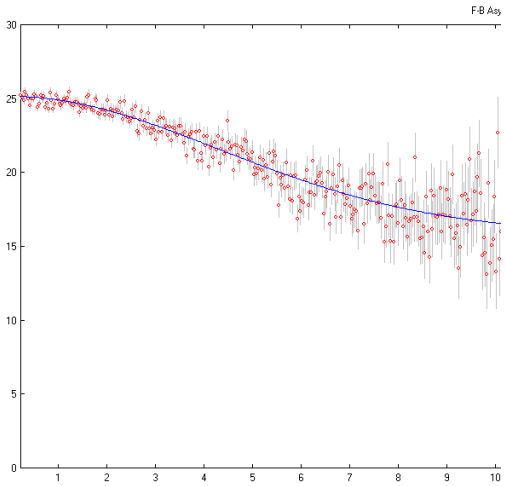

Figure 3.38: Time spectrum for CIGS at T = 10K and LF = 5 G. The line is a fit with a Gaussian relaxation.

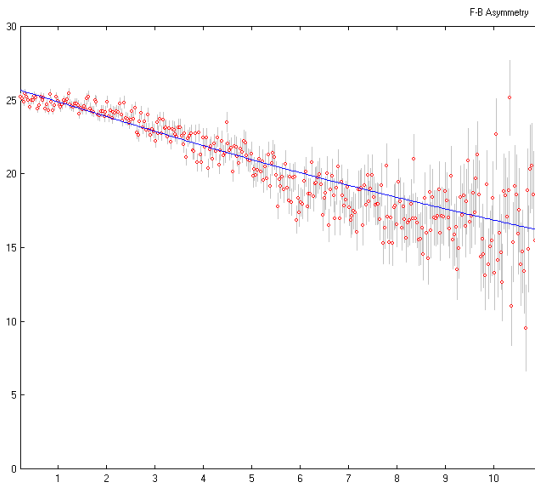

Figure 3.39: Time spectrum for CIGS at T = 10K and LF = 5 G. The line is a fit with a Lorentzian relaxation.

3.6.2 Fit results

In figures 3.40 and 3.41 we show the fits results for the fractions (after normalizing to the Ag fraction) and for the relaxation, respectively. The gaussian-damped component is quenched at about 25 G, which is sugestive of nuclear interactions. The strenght and field dependence of the relaxation in Fig. 3.41 suggest however that elctronic interactions may also play a role.

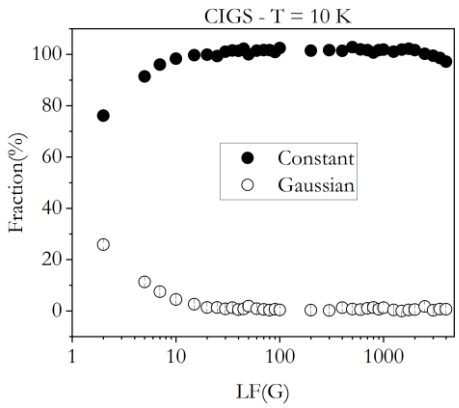

Figure 3.40: LF dependence of the fractions.

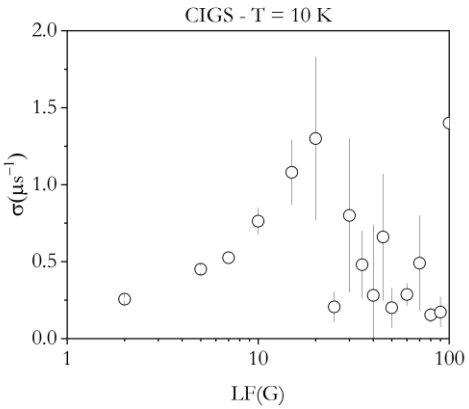

Figure 3.41: LF dependence of the relaxation of the Gaussian-damped component.

3.7. CZTS repolarization at T = 10 K.

3.7.1 About the shape of the relaxing component.

In CZTS, for the corresponding repolarization at T = 10 K, we also tried both Lorentzian and Gaussian shape for the relaxing component (Figs. 3.42 and 3.43 below). The shape is now clearly closer to Lorentzian, unlike what is observed for CIGS at the same temperature. This is clear evidence that the nature of this relaxing component is different in CZTS and CIGS. In CIGS we may have a more important contribution from nuclear moments, whereas in CZTS the origin of the relaxation is likely to have a more important electronic contribution. Something to be further discussed.

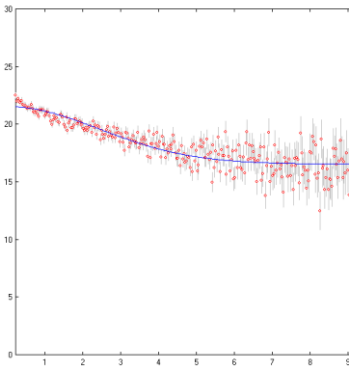

Figure 3.42: Time spectrum for CZTS at T = 10K and LF = 5 G. The line is a fit with a Gaussian relaxation.

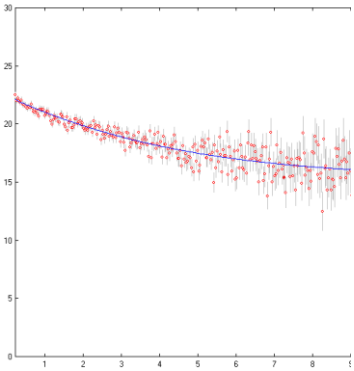

Figure 3.43: Time spectrum for CZTS at T = 10K and LF = 5 G. The line is a fit with a Lorentzian relaxation.

3.7.2 Fit results

In figures 3.44 and 3.45 we show the fits results for the fractions (after normalizing to the Ag fraction) and for the relaxation, respectively. We now observe a second step at high fields (c. 1kG), and a relaxation which seems to be constant above 10 G. All this suggests the presence of electronic interactions.

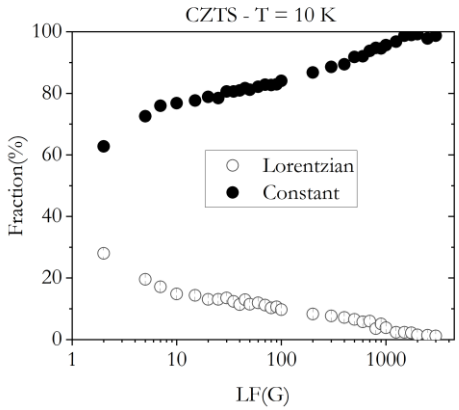

Figure 3.44: LF dependence of the fractions at T = 10 K. The repolarization is two-stepped, with one step around 10 G (nuclear moments?) and another around 1 kG.

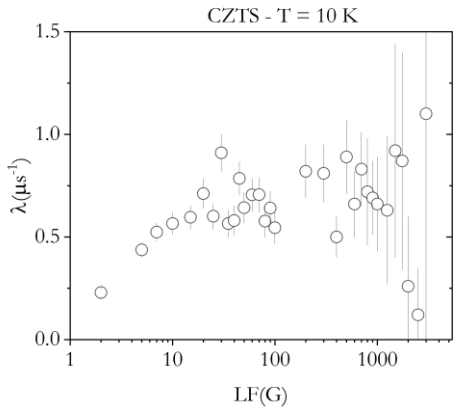

Figure 3.45: LF dependence of the relaxation of the Lorentzian-damped component at T = 10 k. The relaxation seems to be reasonably constant at around 0.6 μs^{-1}.

3.7.3 Repolarization at higher temperatures (T = 100 K and T = 175 K)

Figures 3.46, 3.47, 3.48 and 3.49 show the corresponding fit results for the repolarization curve in CZTS at T = 100 K and T = 175 K. Figures 3.50 and 3.51 gather all temperature results for the fraction and relaxation, respectively. Some variation in the fraction is observed in the 10-

1000 G region, but the final fraction at the highest field seems to be the same at all temperatures; the relaxation seems to be reasonably the same for all temperatures.

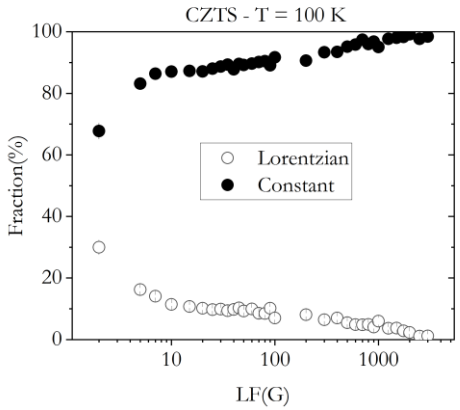

Figure 3.46: LF dependence of the fractions at T = 100 K.

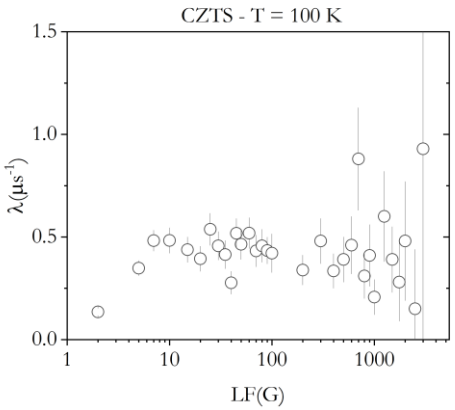

Figure 3.47: LF dependence of the relaxation of the Lorentzian-damped component at T = 100 K.

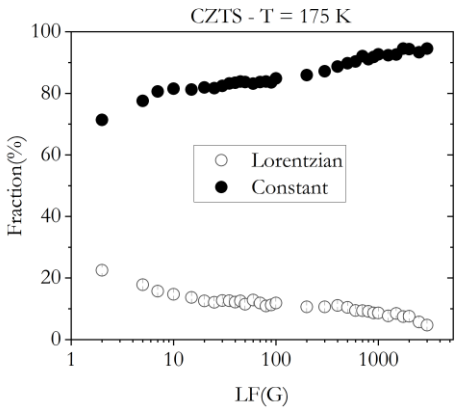

Figure 3.48: LF dependence of the fractions at T = 175 K.

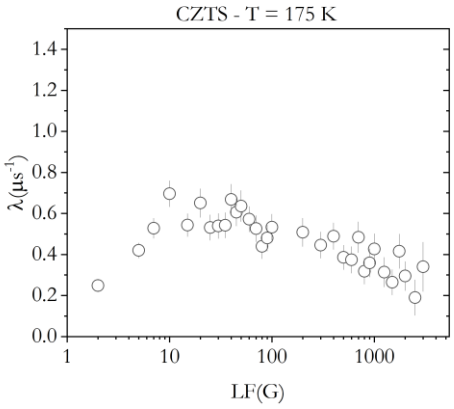

Figure 3.49: LF dependence of the relaxation of the Lorentzian-damped component at T = 175 K.

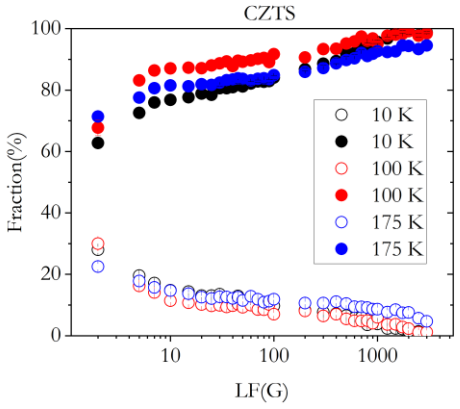

Figure 3.50: LF dependence of the fractions at the different temperatures.

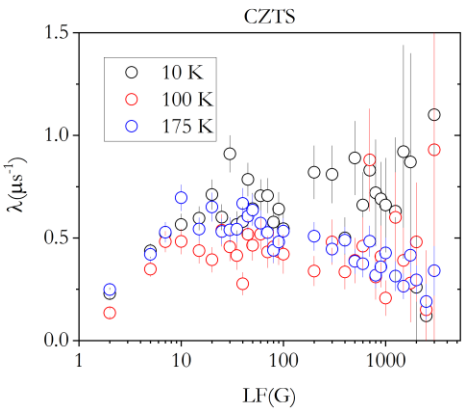

Figure 3.51: LF dependence of the relaxations at the different temperatures

3.8. Temperature dependence in low transverse fields

We present in this and in the next section the results of temperature dependent measurements in low transverse fields (this section) and in zero-field. These are bound to clarify the thermal stability of the muon configurations found. However, as we shall see, the zero-field technique is much more sensitive. However, as will discuss in Chapter 4, the transverse field measurements at low fields have information which is not available in any other experiment. The measurements were done at B = 5 G for CIGS and CZTS. For CZTS only, temperature dependence at B = 20 G was also performed.

3.8.1 CIGS

The analysis of the temperature dependence of CIGS at TF = 5G was performed using the same model for the sample holder as in Section 3.2.1 (complex signal with 3 components: oscillation +relaxation+baseline) and a Gaussian relaxing component for the sample. The fits were performed in the 0-23μs time window, with a bunch of 2 at an automatically adjusted background. For T ≥ 550K, the relaxation had to be fixed to zero. The calibration of the maximum asymmetry was performed as explained in Section 3.2.3. The corresponding temperature dependence of the diamagnetic fraction and relaxation are shown in Fig. 3.52 and 3.53, respectively.

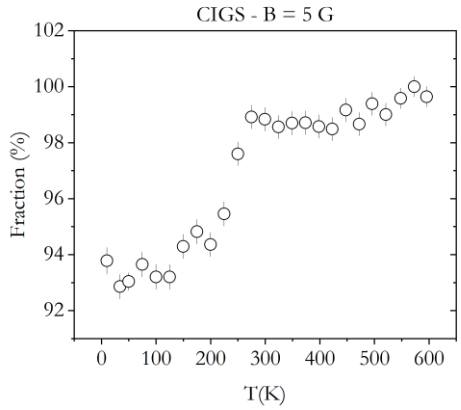

Figure 3.52: Temperature dependence of the diamagnetic fraction in CIGS in TF = 5G. A complete recovery of the 6% missing fraction is observed above 200 K.

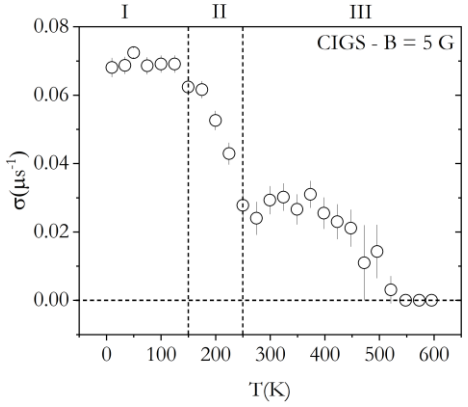

Figure 3.53: Temperature dependence of the Gaussian diamagnetic relaxation in CIGS in TF = 5G. Three distinct temperature regions are visible:

I. Static muon (T < 150 K)
II. Motional narrowing (150 <T <250 K)
III. Trapping and detrapping (T >250 K)

3.8.2. CZTS

I) TF = 5 G

The analysis of the temperature dependence of CZTS at TF = 5G was performed in the same way as for CIGS: sample holder with complex signal with 3 components: oscillation +relaxation+baseline; sample modelled using a Gaussian relaxing component. The fits were performed in the 0-23μs time window, with a bunch of 2 at an automatically adjusted background. For T ≥ 373 K, the relaxation had to be fixed to zero. The calibration of the maximum asymmetry was performed as explained in Section 3.2.3. The corresponding temperature dependence of the diamagnetic fraction and relaxation are shown in Fig. 3.54 and 3.55, respectively. A possible thermal spike effect is observed in Fig. 3.54 for temperatures below T = 200 K: this will be discussed in Chapter 4.

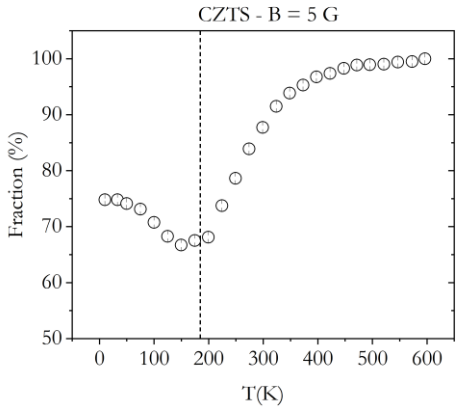

Figure 3.54: Temperature dependence of the diamagnetic fraction in CZTS in TF = 5G. Two distinct temperature regions are visible, above and below T = 185 K:
I. T < 185 K: possible thermal spike;
II. T > 185 K: recovery of diamagnetic fraction

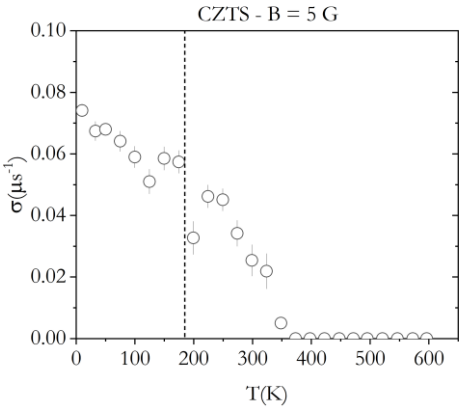

Figure 3. 55: Temperature dependence of the Gaussian diamagnetic relaxation in CZTS in TF = 5G. There is a general decreasing trend of the relaxation with increasing temperature, which is perhaps more intense for T > 185 K.

II) TF = 20 G

A temperature dependence at TF = 20 G was begun in the last night of this experiment, which had to be stopped at T = 230 K at the end of the beamtime. The analysis was performed as above (f_1 = 0.2774 MHz, ϕ_1 = − 6.19 deg, for the sample holder). The corresponding temperature dependence of the diamagnetic fraction and relaxation are shown in Fig. 3.56 and 3.57, respectively. They are compared with the corresponding temperature dependence curves at TF

= 5 G in Fig. 3.58 and Fig. 3.59 respectively. Clearly differences are observed that will be discussed in Chapter 4.

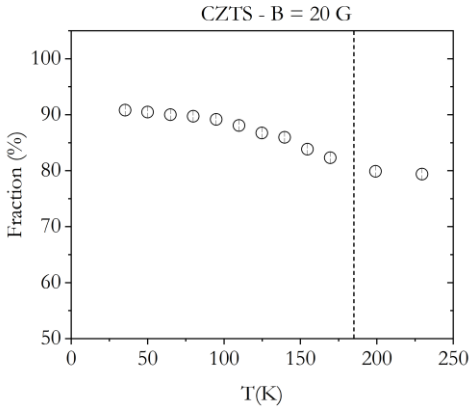

Figure 3.57: Temperature dependence of the diamagnetic fraction in CZTS in TF = 20 G, up to 230 K. The presumed thermal spike region is completely visible up to 200 K.

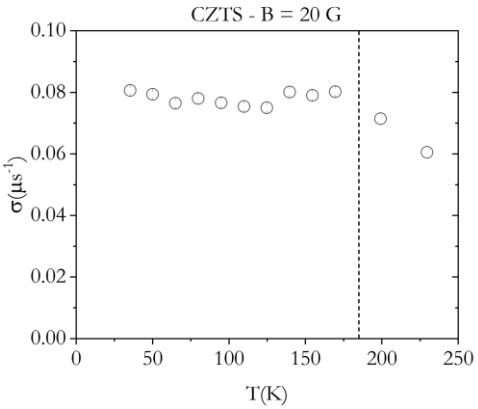

Figure 3.58: Temperature dependence of the Gaussian diamagnetic relaxation in CZTS in TF = 20 G, up to 230 K. The relaxation is approximately constant.

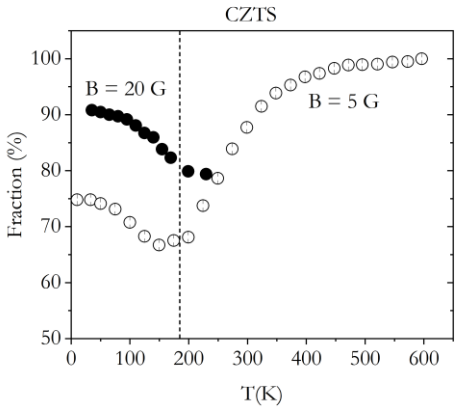

Figure 3.59: Temperature dependence of the fractions at the different fields.

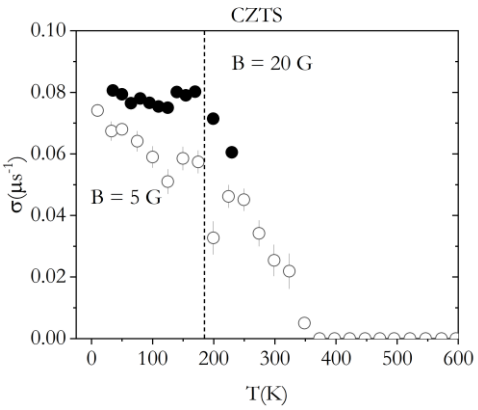

Figure 3.56: Temperature dependence of the relaxations at the different fields.

3.9 Repetition of TF dependence at T = 400 K

We tried a second TF dependence at T = 400 K. When looking now to Fig. 3.58, which shows a diamagnetic fraction of close to 100 % at this temperature, this measurement is obviously irrelevant. However, Fig. 3.58 was obtained only now after a long and painful estimation of the maximum asymmetry in the sample. In Fig. 3.60 we show the TF dependence of the diamagnetic fraction at T = 400 K, which is consistently constant at about 96.7(1)%, as (now) expected. The fits were obtained by fixing the relaxation to zero as before (Cf. Fig. 3.59). Nevertheless, this measurement indicates that at 400 K the diamagnetic fraction is about 3.3% smaller than at 600 K (which is being used as reference for maximum asymmetry)

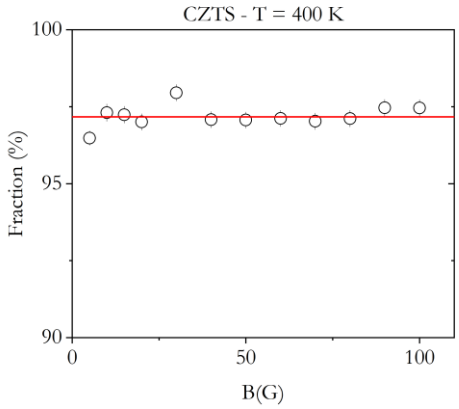

Figure 3.60: TF dependence of the diamagnetic fraction in CZTS at T = 400 K. The fraction is constant with field at 97.2(1)%.

3.10. Temperature dependence at zero field (ZF).

We now present the temperature dependence of the zero field measurements. As before, the calibration of the sample holder signal is discussed, before presenting the experimental data for CIGS and afterwards for CZTS.

3.10.1 Sample holder

The signal from the sample holder was calibrated at ZF, as before, from a measurement using a dummy hematite sample. In order to analyze this measurement, we used the alpha information from the corresponding measurement at TF = 100 G: $\alpha = 1.19$.

The zero-field run was fitted in the 0-20 μs window with bunch = 2. The data from the sample holder, shown in figure 3.61, are reasonably described by a single Lorentzian damped component, with the following parameters: A = 6.785 (58), $\lambda = 0.0772$ (35) μs^{-1}.

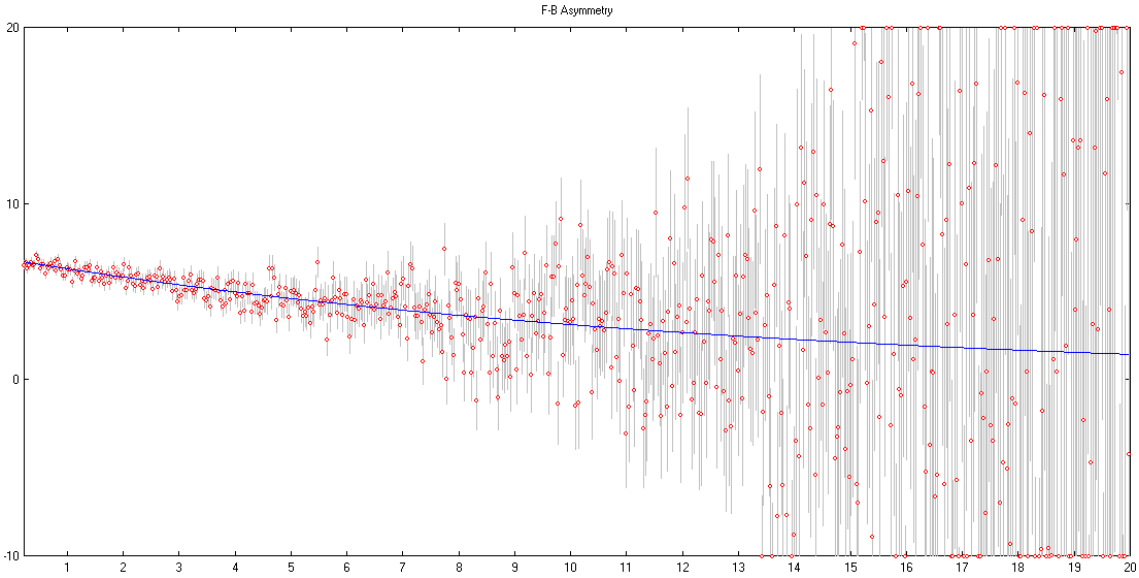

Figure 3.61: Data from the sample holder at ZF, obtained using a dummy hematite sample. A relaxing component is observed.

3.10.2 Calibration of the maximum asymmetry using the silver sample.

In order to calibrate the maximum asymmetry, we used as before a silver sample. The alpha parameter was fixed to $\alpha = 1.025$. (The analysis to Ag indicates a slight dependence of alpha with TF, between 1.0252 (12) for TF = 7.5 G and 1.02382 (67) for TF = 100 G; for TF < 20 G, alpha is however consistently close to 1.025).

In the fit to the ZF (Fig. 3.62), we tried to fix the contribution of the sample holder to the values indicated above in Section 3.10.1 (Lorentzian component with A = 6.785 (58), $\lambda = 0.0772$ (35) μs^{-1}). However, the data are clearly incompatible with the presence of such a large relaxing component. This seems to indicate that the silver sample covered a larger area than the dummy hematite sample, which is likely true. We therefore allowed the asymmetry of the Lorentzian damped component to vary. The data were therefore fitted with two components: a constant + a Lorentzian component with the relaxation fixed to $\lambda = 0.0772$ (35) μs^{-1}. We obtained a reduced value of asymmetry $A_{lor} = 1.48$ (18) for the Lorentzian component and $A_{const} = 23.22$ (15) for the constant component, which we assign to Ag.

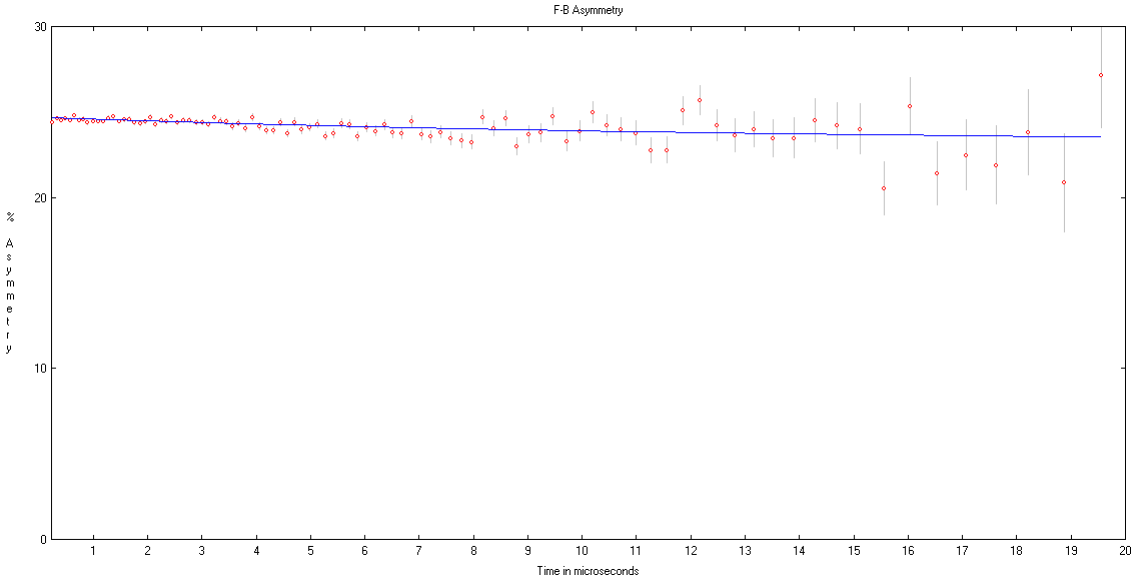

Figure 3.62: Data from the Ag sample holder at ZF. A relaxing component corresponding to muons stopping in the sample holder is observed. For visualization purposes only, we adopted a variable binning, but the fit was performed with a bunch of 2.

3.11. CIGS.

3.11.1 Modeling the sample holder.

In order to check the contribution of the sample holder to the CIGS data, we analyzed the ZF point at T = 300 K, where the relaxing part of the data clearly constitutes a small contribution. This relaxing component is not compatible with A = 6.785, which again indicates that the CIGS sample is likely to be larger than the dummy hematite sample. Unlike what happens in the Ag case, we may have a relaxing contribution from the sample itself, so it is not so easy to obtain the contribution from the sample holder. We have therefore assumed that the contribution of the sample holder is the same as for the calibration with Ag (A = 1.48, $\lambda = 0.0772\ \mu s^{-1}$). In a future reanalysis, we may try to free this asymmetry, in order to try to obtain a refined value; the present analysis nevertheless contains the essential features.

3.11.2 Temperature dependence at ZF

The data were fitted in the 0-23 μs time window, with a bunch = 2, α = 1.25 (TF = 20 G), and an automatically adjusted background. We initially verified the existence of two basically distinct regimes: above T = 300 K, the data are adequately described with a single gaussian relaxing component (plus sample holder); below T = 300 K, an additional non-relaxing component is needed, and the data can be fitted with it in the full temperature range. We have

therefore fitted the data in the full temperature range using these two components (constant plus gaussian), and the sample holder.

We have initially calculated the fractions associated to each component by comparing to the silver asymmetry. However, we verified that we then obtain a total fraction slightly exceeding 100%. We have therefore used the average total asymmetry (A_{tot} = 23.59 (2)) as the reference for the maximum asymmetry in CIGS. The corresponding temperature dependence of the diamagnetic fraction and relaxation are shown in Fig. 3.63 and 3.64, respectively.

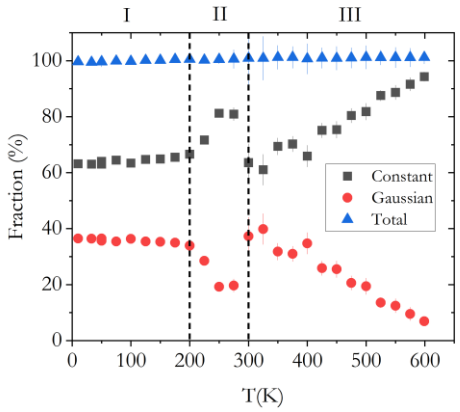

Figure 3.63: Temperature dependence of the fractions observed at ZF in CIGS. The full muon polarization is observed at all temperatures. Three distinct regimes are observed, for temperatures: below 200 K (I), between 200 K and 300 K (II) and above 300 K (III).

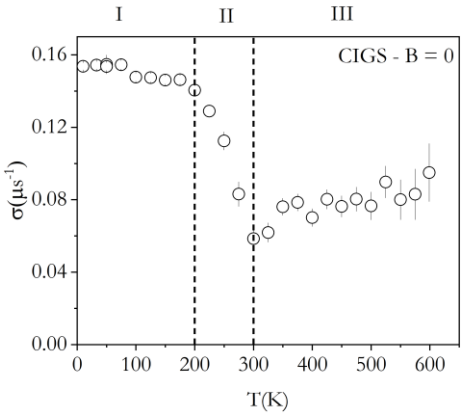

Figure 3.64: Temperature dependence of the relaxation of the Gaussian relaxing component observed in CIGS at ZF. The same temperature regimes are observed, likely corresponding to: static muon (I), motional narrowing (II) and trapping / detrapping (III).

3.12 CZTS

The contribution of the sample holder was modelled in the same way as in CIGS (A = 1.48, λ = 0.0772 μs^{-1}), after we verified that the data at T = 300 K are not compatible with a larger value A = 6.785 of the relaxing component.

The data were fitted in the 0-23 μs time window, with a bunch = 2, α = 1.025, TF = 20 G, and an automatically adjusted background. We again initially verified the existence of two basically distinct regimes: above T = 275 K, the data are adequately described with a single gaussian relaxing component (plus sample holder), although we can fit a constant plus a gaussian as in CIGS.

Below T = 275 K, not only an additional non-relaxing component is needed as in CIGS, but also a fast-relaxing component is clearly visible, particularly at lower temperatures, as shown in Fig. 3.65. This fast-relaxing component was found to be adequately described by a Lorentzian shape. We have therefore fitted the data with the following model:

i) Lorentzian plus constant plus gaussian (plus sample holder) for T < 275 K;

ii) Constant plus gaussian (plus sample holder) for T >275 K.

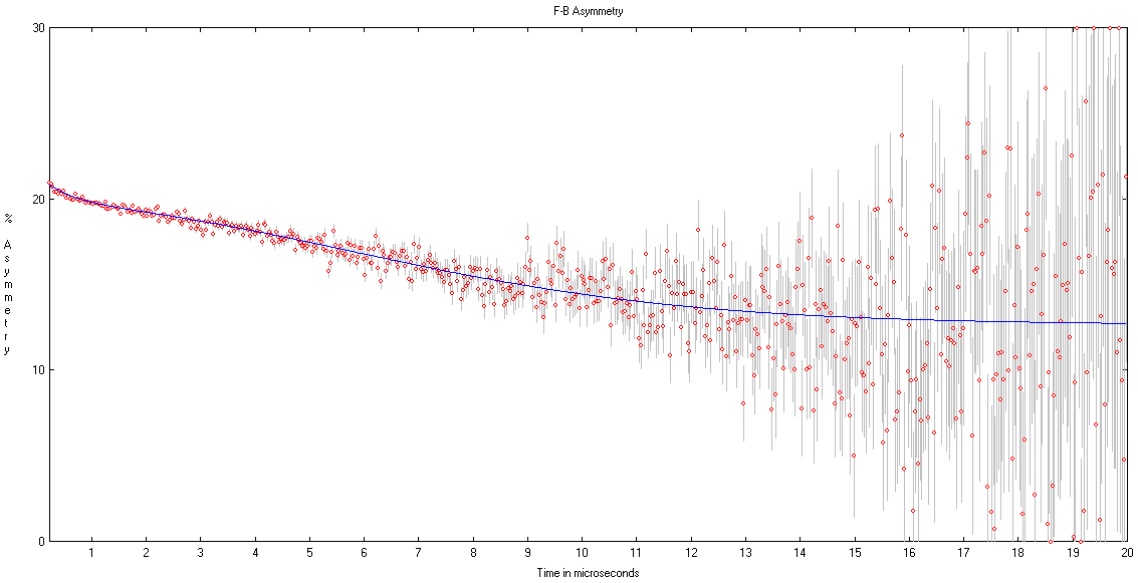

Figure 3.65: μSR spectrum at B = 0 T, T = 175 K in CZTS. A additional relaxing component is visible at shorter times.

We have initially calculated the fractions associated to each component by comparing to the silver asymmetry. However, we verified that we then obtain a total fraction slightly exceeding 100% at the highest temperatures (470 – 600 K). We have therefore used the average total asymmetry between 470 K and 600 K (A_{tot} = 23.90 (1)) as the reference for the maximum asymmetry in CZTS. These fractions are represented in Fig. 3.66, and the corresponding relaxations are shown in Figs. 3.67 and 3.68.

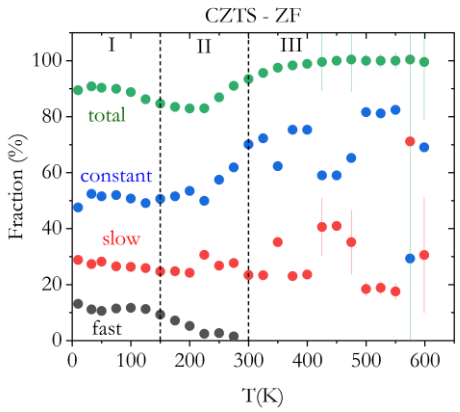

Figure 3.66: Temperature dependence of the fractions observed at ZF in CZTS. As in CIGS, three distinct regimes are observed, for temperatures: below around 150 K (I), between 150 K and 300 K (II) and above 300 K (III). However, the full muon polarization is observed only above T = 300 K. The behavior below T = 150 K is suggestive of a thermal spike effect.

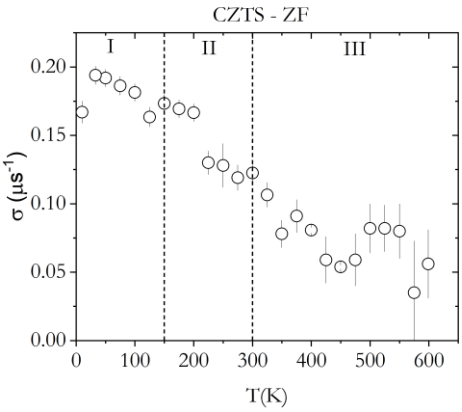

Figure 3.67: Temperature dependence of the relaxation of the Gaussian relaxing component observed in CZTS at ZF. The same temperature regimes as in CIGS are probably also present, although in a less clear way, likely corresponding to: static muon (I), motional narrowing (II) and trapping / detrapping (III).

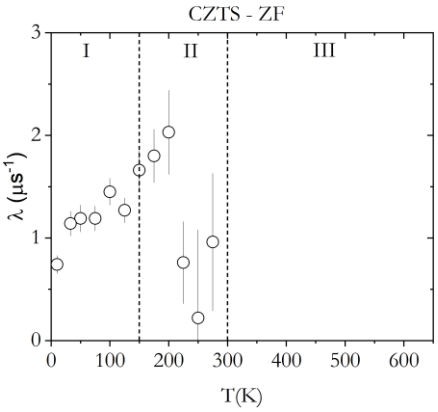

Figure 3.68: Temperature dependence of the relaxation of the Lorentzian relaxing component observed in CZTS at ZF. This component is observed up to T = 300 K only. The probable presence of a thermal spike effect below T = 150 K (Fig. 3.65) and of muon diffusion above T = 200 K (Fig. 3.66 and Fig. 67) suggest that this component is the thermal spike counterpart of the constant component in Fig. 3.65.

Chapter 4: Discussion

4.1. Introduction

We now address the discussion of the experimental data presented in the previous chapter, in the context of the state-of-the-art presented in Chapter 2. In order to start the discussion we recall the basic hydrogen configurations obtained by Marinopoulos *et al*. [Mar+21], using *ab-initio* methods, for the ternary $CuInSe_2$ and for $Cu(In_{0.8125}Ga_{0.1875})Se_2$ (CIGS). The lowest energy positively charged configuration is found near a bond center (BC) site of the Cu-Se bond (Fig.4.1). The lowest energy neutral hydrogen state is found at an interstitial position (Fig. 4.2).

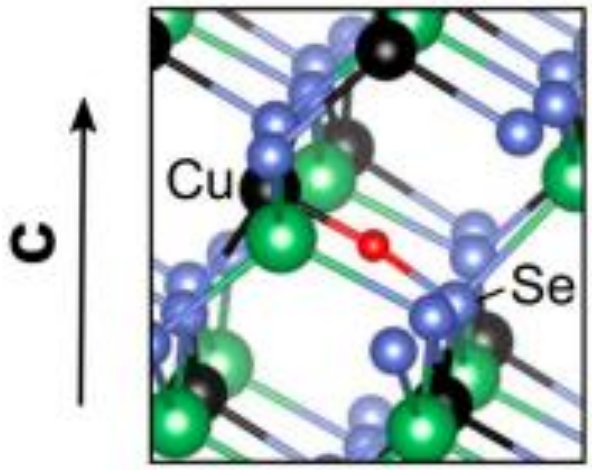

Figure 4.1: Atomistic structure of the lowest energy positively charged hydrogen configuration in $CuInSe_2$. Hydrogen resides near the BC site of the Cu– Se bond. (From ref. [Mar+21])

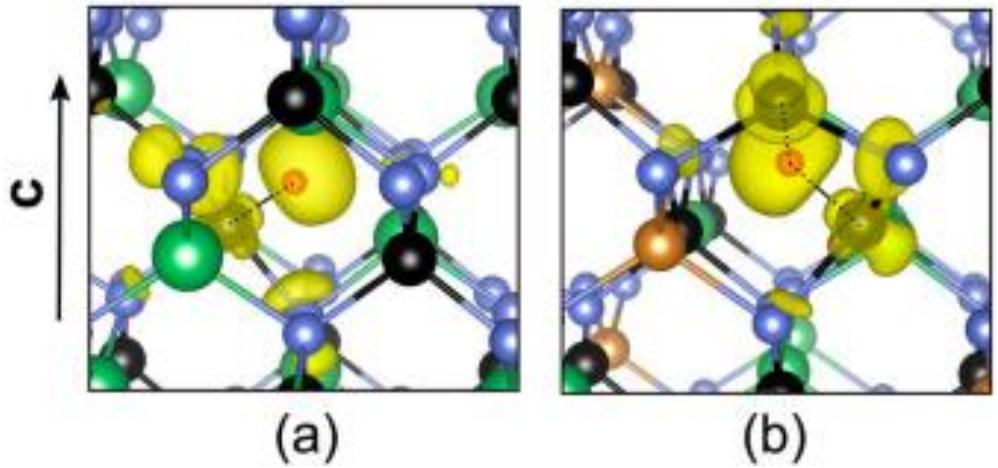

Figure 4.2: Atomistic structures and electron-spin densities (in yellow) of the lowest-energy interstitial neutral states of hydrogen. (a) H^0 interstitial in $CuInSe_2$. (b) H^0 interstitial in CIGS with x=0.1875. The lines connect the hydrogen nucleus to its nearest copper neighbors. The densities are shown for an iso-surface value of 0.002 e $Å^{-3}$. The view is perpendicular to the chalcopyrite tetragonal c axis. (From ref. [Mar+21])

These calculated configurations constitute a very helpful guide for the interpretation of the μSR results. We note however that a full understanding of the experimental data cannot be done exclusively with the lowest energy configurations in "pure" materials, since not only defects are bound to play an important role in chalcopyrite semiconductors, but also higher energy configurations must be taken into account when implanting muons with a high kinetic energy (4 MeV).

4.2. Overview of the components in CZTS and CIGS with ZF

We begin the discussion of the experimental data with the rich information obtained through zero field measurements, where the different relaxing components are more easily separated. We first discuss the CZTS measurements, and then CIGS.

4.2.1 CZTS

We recall Fig. 3.66 and 3.67, which we reproduce again for an easier reference (Fig. 4.3 and 4.4).

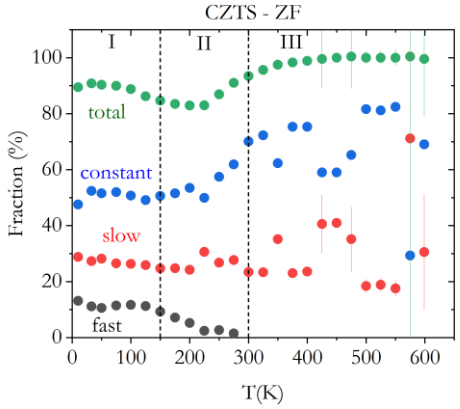

Figure 4.3: Temperature dependence of the fractions observed at ZF in CZTS. As in CIGS, three distinct regimes are observed, for temperatures: below around 150 K (I), between 150 K and 300 K (II) and above 300 K (III). However, the full muon polarization is observed only above T = 300 K. The behavior below T = 150 K is suggestive of a thermal spike effect.

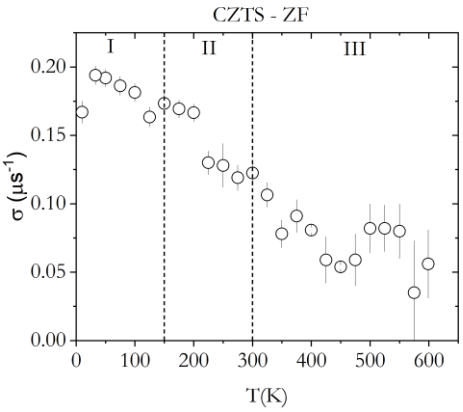

Figure 4.4: Temperature dependence of the relaxation of the Gaussian relaxing component observed in CZTS at ZF. The same temperature regimes as in CIGS are probably also present, although in a less clear way, likely corresponding to: static muon (I), motional narrowing (II) and trapping / detrapping (III).

Slow component. Fig. 4.4 tells us that the slowly relaxing component has a relaxation around 0.18(2) μs^{-1} at low temperatures, which starts to decrease with increasing temperature above T = 150 K and seems to level around 0.05(2) μs^{-1} for temperatures above T = 300 K. The fraction of muons stopping in this configuration remains however apparently constant with temperature at around 30(5)% (the fluctuations observed in Fig. 4.3 are attributed to statistical fluctuations

in these complex fits). The value of the relaxation at low temperatures is consistent with that observed previously in TF measurements [Alb+18], after taking into account that the relaxation Δ at zero field is expected to be larger than the relaxation σ at transverse field: $\Delta \sim 1.58\sigma$ [Vil02]. We therefore assign this slowly relaxing diamagnetic component to muons stopping as Mu^+ in a bound configuration, as that of Fig. 4.1. We attribute the decrease of the relaxation above T = 200 K to motional narrowing [Vil02] due to the onset of muon diffusion. However, as observed previously in chalcopyrite semiconductors [Vil02], the relaxation does not drop to zero at high temperatures. Instead, it stabilizes at around 0.07 us-1 above 300 K, which is consistent with muons stopping in metal vacancies [Vil+03b]. This points to a very high concentration of defects in the sample.

Fast component. The fast-relaxing component in Fig. 4.3 clearly corresponds to a transient configuration which becomes unstable for temperatures above T = 150 K as observed before [Alb+14] and confirmed in Fig. 4.5. This component only corresponds to a very small fraction (about 15% below T = 100 K) of the stopped muons. This diamagnetic-like configuration has been recently interpreted as a muonium transition state corresponding to a paramagnetic state with small and fluctuating hyperfine interaction due to a highly delocalized electronic wave function [Vil+23]. In this interpretation, it corresponds to muons stopping in an interstitial configurations such as that Fig. 4.2, but in a non-relaxed electronic wave function. From this transient excited configuration, muonium can afterwards relax to the lowest energy configurations (such as those shown in Fig. 4.1 and 4.2).

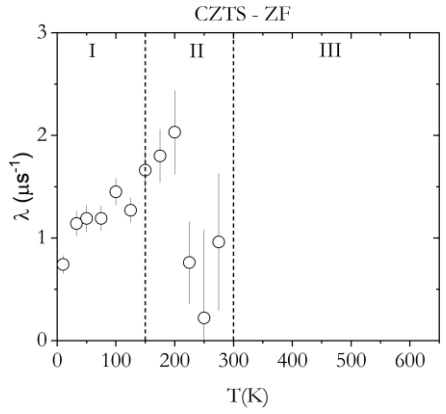

Figure 4.5: Temperature dependence of the relaxation of the Lorentzian relaxing component observed in CZTS at ZF. This component is observed up to T = 300 K only. The probable presence of a thermal spike effect below T = 150 K (Fig. 4.3) and of muon diffusion above T = 200 K (Fig. 4.4 and Fig. 4.5) suggest that this component is the thermal spike counterpart of the constant component in Fig. 4.3.

Non-relaxing component. However, the dominant configuration in the zero field measurements shown in Fig. 4.3 has no apparent relaxation ("constant" component), which is very puzzling since the high concentration of nuclear moments in CZTS implies a non-zero value for the relaxation of static muons, even at sites relatively distant from the nearest nuclei. The absence

of relaxation, even that created by nuclear moments, points to a fast spin exchange situation [Dua07]; all this points to muons stopping in interstitial sites, eventually close to defects, which are expected to be abundant in these materials [Kum+15, Mcg+21, Vio+22]. We therefore assign this component to muons stopping at interstitial sites as those shown in Fig. 4.2 but with very strong spin dynamics so that only a non-relaxing component is observed. This component amounts to nearly 70% above room temperature.

Below room temperature, there is clearly a conversion process to this constant component, involving both the fast relaxing component (about 15% below T = 100 K) and the missing fraction (unobserved muons, around 10% below T = 100 K). As we have seen in Chapter 3 (Section 3.9) and shall discuss below, the repolarization of the missing fraction indicates the presence of an electronic compact muonium state as that presented in Fig. 4.2. All this suggests that indeed both the fast relaxing component, the missing fraction and the non-relaxing component corresponds to muons stopping as muonium in interstitial sites: the fast component as a transient muonium configuration, the missing fraction as static compact muonium in the intrinsic lowest energy site, and finally the non-relaxing component as muonium in interstitial site(s) with very fast spin dynamics possibly due to strong interaction with defects.

4.2.2 CIGS

In order to discuss the corresponding zero field measurements, we recall Figs. 3.63 and 3.64, which we reproduce again for an easier reference (Fig. 4.6 and 4.7). We note that only two components are observed in the zero field measurements: a slow-relaxing component and a non-relaxing component (gaussian and constant components in Fig. 4.6, respectively). As in CZTS and previously studied chalcopyrite systems [Vil02, Vil+03b] the temperature dependence of the relaxation of slowly relaxing component indicates motional narrowing between T = 200 K and T = 300 K and hints of trapping for temperatures above T = 300 K. The temperature dependence of the fractions (Fig. 4.6) clearly indicates that these remain approximately constant for temperatures below T = 200 K, whereas a conversion from the slowly relaxing component to the non-relaxing component seems to occur for temperature above T = 400 K. A fluctuation of the fractions is visible between T = 200 K and T = 300 K, but this is possibly an artifact due to poor fitting in the motional narrowing region and we do not attribute any physical meaning to it.

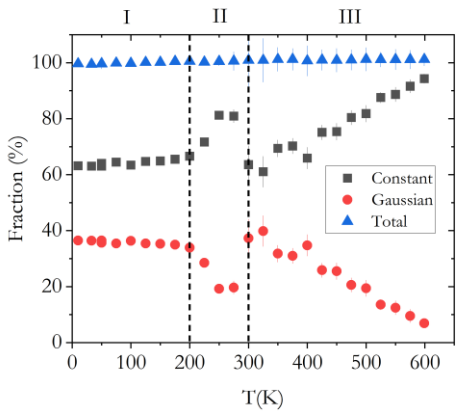

Figure 4.6: Temperature dependence of the fractions observed at ZF in CIGS. The full muon polarization is observed at all temperatures. Three distinct regimes are observed, for temperatures: below 200 K (I), between 200 K and 300 K (II) and above 300 K (III).

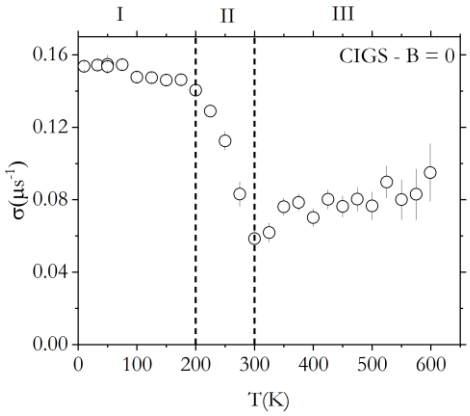

Figure 4.7: Temperature dependence of the relaxation of the Gaussian relaxing component observed in CIGS at ZF. The same temperature regimes are observed, likely corresponding to: static muon (I), motional narrowing (II) and trapping / detrapping (III).

The physical interpretation of the zero field measurements in CIGS therefore proceeds in a similar way as that of CZTS: we assign the slowly relaxing component to muons stopping in a bound muonium configuration as that of Fig. 4.1 and the non-relaxing component to muons subject to fast spin relaxation and stopping in interstitial sites (as those in Fig. 4.2).

An important difference of these CIGS zero field measurements with respect to the corresponding CZTS measurements relates to the fact that the full muon polarization is observed at all temperatures (total fraction of 100% at all temperatures in Fig. 4.6, i.e., no "missing fraction"), as well as to the fact that the fast relaxing component is not observed. As we shall discuss below, we have other indirect evidence for the presence of the fast relaxing component, so that the fact that it is not observed in these measurements seems to indicate that its life time is much shorter in CIGS than in CZTS. On the other hand, the observation of full muon polarization (no "missing fraction") seems to indicate that all muons stopping in interstitial sites have a strong interaction with defects.

Another important difference relates to the thermal instability of the slow relaxing component, which apparently converts to the non-relaxing for temperatures above T = 400 K, where the muon is diffusing rapidly through the sample, encountering defects. Trapping in defects where the muon is subject to a fast spin relaxation is likely to be the most probable explanation; in fact, the simple conversion to the "intrinsic" interstitial site, albeit with the fast spin relaxation, seems to be ruled out by theoretical calculations which indicate that the bound configuration

has the lowest formation energy in p-type chalcopyrites [Mar+21]. All this points out that defects are probably more relevant in the disordered CIGS system than in CZTS.

4.3 Interstitial configuration

The longitudinal field measurements presented in Section 3.9 constitute an invaluable contribution for the characterization of the paramagnetic components that are not directly accessible otherwise. In these measurements a magnetic field is applied parallel to the direction of the initial spin polarization of the muon beam (longitudinal geometry). For high magnetic fields the Zeeman interaction is dominant, so that the muon spin polarization is quenched; but for low magnetic fields, any existing hyperfine interaction may lead to muonium precession frequencies responsible for the depolarization of the muon spin. As we have seen in Section 2.4, field dependent measurements (repolarization measurements) therefore allow the determination of the hyperfine interaction.

As we have seen in Section 3.9 and have discussed in the Section 4.2 above, the full muon polarization is observed in the CIGS measurements. We will henceforth focus on the CZTS results.

We analyzed the repolarization curve in Fig. 3.43 with the model of Eq.2.12 presented in Section 2.4 (Fig. 4.8). The analysis with a single hyperfine interaction, shown as a doted curve in Fig. 4.8, reveals the presence of a 1.6(4) GHz hyperfine interaction, amounting to about 29(7)% of the muon spin polarization. This is an expected result taking into account the zero field results discussed above, where the sum of the slowly relaxing diamagnetic and of the non-relaxing diamagnetic-like components amounts to about 75(5)% , whereas the sum of the paramagnetic fast relaxing component and missing fraction amounts to about 25(5)%.

The dotted curve in Fig. 4.8 does not however describe the experimental data for fields below a few hundred Gauss. We have therefore reanalyzed the data in Fig. 4.8 introducing a second hyperfine interaction. The result of the fit is shown in Fig. 4.8 as a full red curve, which adequately describes the data in the entire field range above B = 10 G, with A_1 = 1.5(1) GHz (with a repolarized fraction of 15(1)%) and A_2 = 102(16) MHz (with a repolarized fraction of 8(1)%). We attribute the further depolarization observed for fields below 10 G to effects of the nuclear magnetic moments. The full meaning of this result is not entirely clear and requires a deeper analysis that is out of the scope of this dissertation: in particular, a clear separation of the repolarization of the fast component and that of the missing fraction likely requires the

development of muonium dynamics models [Pat88]. This results nevertheless clearly shows the presence of an atomic-like muonium state with a hyperfine interaction around 1.5 GHz (as predicted in Fig. 4.2). The lower hyperfine interaction around 100 MHz may either correspond to anisotropy [Pra97] or to a manifestation of the delocalized wave function associated to the transition state.

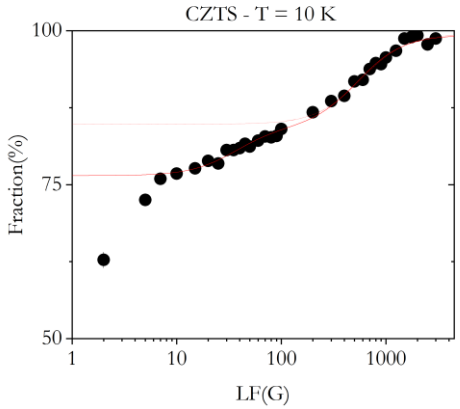

Figure 4.8: LF dependence of the constant fraction in CZTS at T = 10 K (Cf. Fig. 3.44). The dotted curve is a fit with a single isotropic muonium component and the full red curve is a fit with two components, as explained in the text.

4.4 Transition state

As we have mentioned in Section 4.2 the fast component observed in the zero field measurements in CZTS likely corresponds to a muonium transition state with a small and fluctuating hyperfine interaction due to a highly delocalized electronic wave function [Vil+23]. The paramagnetic character of this otherwise seemingly diamagnetic state is reflected in subtle changes in the precession observed in small traverse fields. The measurements shown in Section 3.5 were intended to probe these small effects.

The obtained results were unmistakably positive, but also show remarkable differences between CZTS and CIGS that require further modelling. In fact, in CIGS a clear positive frequency shift is observed (Fig. 3.23, reproduced again below as Fig. 4.9), similarly to the transition state found in ZrO_2 ([Vil+17]) however, in CZTS a prominent phase shift is observed (Fig. 3.29, reproduced again below as Fig. 4.10). These differences require further investigation in order to clarify the characteristics of the transition states in each system.

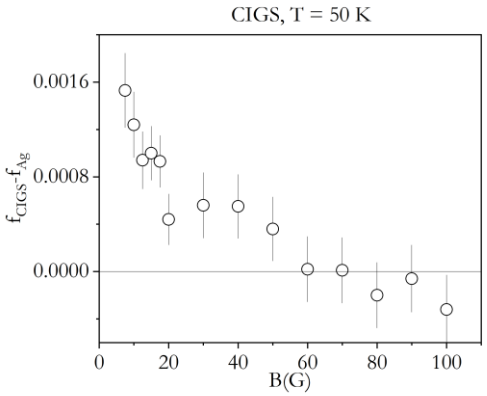

Figure 4.9: Field dependence of the difference between the frequency of the CIGS and silver. A clear frequency shift is observed below 60 G. This is consistent with a hyperfine interaction around 1 MHz.

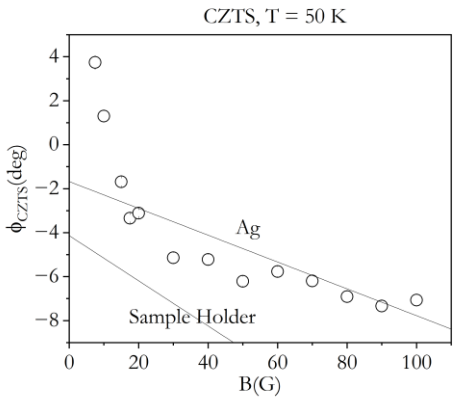

Figure 4.10: Field dependence of the muon phase. The figure also shows the field dependence of the muon phase for Ag and sample holder.

4.5 Muon stopping in defects

We now briefly discuss the evidence pointing to a very strong presence of defects in our samples. As pointed out above, defects play a very important role in chalcopyrite systems [Kum+15, Mcg+21, Vio+22]. Our experimental data have strong indications that indeed muons seem to stop close to defects even at the lowest temperatures (around 10 K), which indicates that the concentration of defects in our samples is much higher than in previously studied chalcopyrite systems [Vil+03, Alb+18]. We only address here CZTS, where a more complete picture can be drawn.

As discussed in Section 4.2, we assign the dominant configuration in the zero field measurements in CZTS to muons stopping in interstitial sites, most likely close to defects. The absence of relaxation points to very strong spin dynamics or even to possible phase segregation (which, although not anticipated, should nevertheless be ruled out by x-ray diffraction measurements to be done in a near future).

The transverse field measurements presented in Section 3.11 seem to point also to a very strong dynamics of the defects morphology. In order to proceed with the interpretation, we first note that these transverse field measurements are much less powerful than the zero-field measurements for the separation of components with small relaxation, so that the non-relaxing component and slowly relaxing component observed in zero-field become impossible to separate and are therefore observed as a single component with the average relaxation. We also

note that the temperature dependences shown in Fig. 4.11 show a minimum just below T = 200 K, which likely corresponds to a thermal spike effect as previously observed [Vil+19].

However, as shown in Fig. 3.58 (that we reproduce below as Fig. 4.11), there is a strong inconsistency with the results of Fig. 3.28 (that we reproduce below as Fig. 4.12): whereas in the field dependent measurements at T = 50 K we observed a field independent fraction of 75% (corresponding to the sum of the non-relaxing component and slowly relaxing component observed in zero-field at T = 50 K), the results summarized in Fig. 4.11 clearly indicate an increase from 75% to 90%, at T = 50 K, between the transverse measurements at B = 5 G and B = 20 G. We note that the temperature dependence at B = 20 G was performed after the joint zero-field and B = 5 G temperature dependence, where the sample was heated up to 600 K. The transverse field dependence at T = 50 K (Fig. 4.12) was also performed before heating the sample up to 600 K. Direct comparison of the two time spectra at T = 50 K, B = 20 G clearly shows an increase of the asymmetry, indicating that the inconsistency is a real effect. Instrumental effects can be discarded. The most likely explanation for this inconsistency is therefore that the heating of the sample up to 600 K performed an annealing that changed de defect morphology and thus the formation probability of the different muon components.

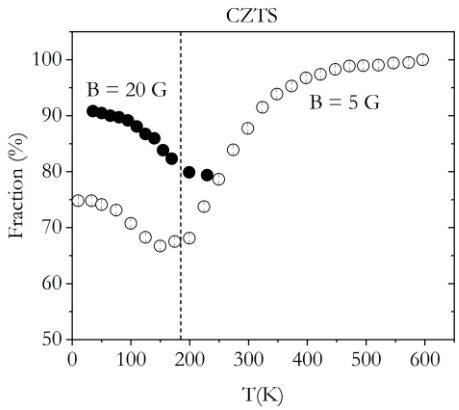

Figure 4.11: Temperature dependence of the fractions at the different fields.

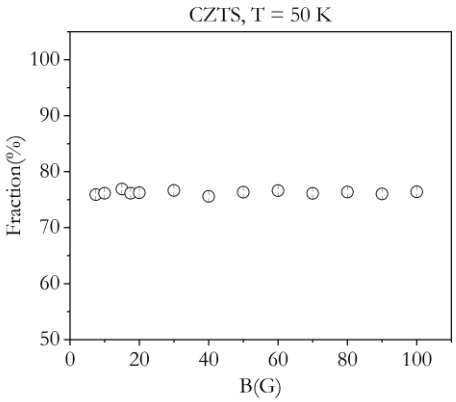

Figure 4.12: Field dependence of the diamagnetic fraction, after comparing the sample asymmetry with that of Ag. The error bars are the simple statistical ones obtained from straight error propagation.

4.6 Concluding Remarks

As a conclusion, we have performed in this work a thorough characterization of the muonium configurations in the chalcopyrite semiconductors CIGS and CZTS: both interstitial muonium and bound muonium are present. A fast relaxing component associated to a transient state in the thermalization process has also been characterized. However, the dominant configuration is a non-relaxing component that we associate to muons stopping at or near defects.

In the end of this work, several questions remain to be clarified, requiring further investigation. An immediate request is that of checking the possible presence of spurious phases in the samples. Moreover, the extremely difficult analysis of the data and the separation of the various components, particularly at zero-fields, may require a deeper analysis taking in to account the physical picture drawn in this work, in order to reduce fitting fluctuations. Also, as we have seen above, the full meaning of the longitudinal field measurements is not entirely clear and requires a deeper analysis in order to try to separate the fast component and the missing fraction. Physical modelling is also needed in order to understand the different behavior of the transition state in CIGS and CZTS.

Bibliography

[Al+22] Al-Ezzi, A. S., & Ansari, M. N. M. (2022). Photovoltaic solar cells: a review. *Applied System Innovation*, *5*(4), 67.

[Alb+14] Alberto, H. V., Vilão, R. C., Gil, J. M., Duarte, J. P., Vieira, R. B. L., Weidinger, A., ... & Salman, Z. (2014, December). Muonium states in Cu2ZnSnS4 solar cell material. In *Journal of Physics: Conference Series* (Vol. 551, No. 1, p. 012045). IOP Publishing.

[Alb+18] Alberto, H. V., Vilão, R. C., Vieira, R. B. L., Gil, J. M., Weidinger, A., Sousa, M. G., ... & Salman, Z. (2018). Slow-muon study of quaternary solar-cell materials: Single layers and p− n junctions. *Physical Review Materials*, *2*(2), 025402.

[Ban+20] Banik, U., Sasaki, K., Reininghaus, N., Gehrke, K., Vehse, M., Sznajder, M., ... & Agert, C. (2020). Enhancing passive radiative cooling properties of flexible CIGS solar cells for space applications using single layer silicon oxycarbonitride films. *Solar Energy Materials and Solar Cells*, *209*, 110456.

[Bar+10] Barkhouse, D. A. R., Gunawan, O., Gokmen, T., Todorov, T. K., & Mitzi, D. B. (2012). Device characteristics of a 10.1% hydrazine-processed Cu2ZnSn (Se, S) 4 solar cell. *Progress in Photovoltaics: Research and Applications*, *20*(1), 6-11.

[Ber+12] Beringer, J., Arguin, J. F., Barnett, R. M., Copic, K., Dahl, O., Groom, D. E., ... & Shaevitz, M. H. (2012). Review of particle physics. *Physical Review D*, *86*(1).

[Bis+23] Biswas, P. K., Yokoyama, K., Adroja, D. T., & Yadav, C. S. (2023). Muon spin relaxation and emergence of disorder-induced unconventional dynamic magnetic fluctuations in Dy $ _ {2} $ Zr $ _ {2} $ O $ _ {7} $. *arXiv preprint arXiv:2303.14426*.

[Blu+22] Blundell, S. J., Blundell, S., De Renzi, R., Lancaster, T., & Pratt, F. L. (Eds.). (2022). *Muon Spectroscopy: An Introduction*. Oxford University Press.

[BOU]https://www.bougerv.com/search?type=product%2Carticle%2Cpage%2Ccollection&options[prefix]=last&q=CIGS*

[Cat+22] Cataldo, M., Clemenza, M., Ishida, K., & Hillier, A. D. (2022). A novel non-destructive technique for cultural heritage: Depth profiling and elemental analysis underneath the surface with negative muons. *Applied Sciences*, *12*(9), 4237.

[Cox09] Cox, S. F. J. (2009). Muonium as a model for interstitial hydrogen in the semiconducting and semimetallic elements. *Reports on Progress in Physics*, *72*(11), 116501.

[Dua07] Duarte, J. P. P. P. (2007). *Study of Hydrogen in Phthalocyanine Semiconductors Using μSr Technique* (Doctoral dissertation, Universidade de Coimbra (Portugal)).

[Fac+20] Fachrizal, R., Shepero, M., van der Meer, D., Munkhammar, J., & Widén, J. (2020). Smart charging of electric vehicles considering photovoltaic power production and electricity consumption: A review. *ETransportation*, *4*, 100056.

[Gar+19] García, A. M., Gallagher, J., McNabola, A., Poyato, E. C., Barrios, P. M., & Díaz, J. R. (2019). Comparing the environmental and economic impacts of on-or off-grid solar photovoltaics with traditional energy sources for rural irrigation systems. *Renewable Energy*, *140*, 895-904.

[Ghe+20] Gheidi, S., Akintola, K., Fang, A. C. Y., Sundar, S., Côté, A. M., Dunsiger, S. R., ... & Sonier, J. E. (2020). Absence of μ SR evidence for magnetic order in the pseudogap phase of Bi 2+ x Sr 2− x CaCu 2 O 8+ δ. *Physical Review B*, *101*(18), 184511.

[Gil+99] Gil, J. M., Mendes, P. J., Ferreira, L. P., Alberto, H. V., Vilão, R. C., de Campos, N. A., ... & Cox, S. F. J. (1999). Modeling hydrogen in CuInSe2 and CuInS2 solar cell materials using implanted muons. *Physical Review B*, *59*(3), 1912.

[Gug20] Guguchia, Z. (2020). Unconventional magnetism in layered transition metal dichalcogenides. *Condensed Matter*, *5*(2), 42.

[Hil+16] Hillier, A. D., Paul, D. M., & Ishida, K. (2016). Probing beneath the surface without a scratch—Bulk non-destructive elemental analysis using negative muons. *Microchemical Journal*, *125*, 203-207.

[Hil+19] Hillier, A. D., Lord, J. S., Ishida, K., & Rogers, C. (2019). Muons at ISIS. *Philosophical Transactions of the Royal Society A*, *377*(2137), 20180064.

[Hil+22] Hillier, A. D., Blundell, S. J., McKenzie, I., Umegaki, I., Shu, L., Wright, J. A., ... & Watanabe, I. (2022). Muon spin spectroscopy. *Nature Reviews Methods Primers*, *2*(1), 4.

[Hit+99] Hitti, B., Kreitzman, S. R., Estle, T. L., Bates, E. S., Dawdy, M. R., Head, T. L., & Lichti, R. L. (1999). Dynamics of negative muonium in n-type silicon. *Physical Review B*, *59*(7), 4918.

[IEA] IEA (2023), World Energy Investment 2023, IEA, Paris https://www.iea.org/reports/world-energy-investment-2023, License: CC BY 4.0

[ISI] https://www.isis.stfc.ac.uk/Pages/Emu-science.aspx

[Kha+23] Khasanov, R., Ramires, A., Grinenko, V., Shipulin, I., Kikugawa, N., Sokolov, D. A., ... & Guguchia, Z. (2023). In-plane magnetic penetration depth in Sr $ _2 $ RuO $ _4 $: muon-spin rotation/relaxation study. *arXiv preprint arXiv:2305.11156*.

[Kie+84] Kiefl, R. F., Holzschuh, E., Keller, H., Kündig, W., Meier, P. F., Patterson, B. D., ... & Denison, A. B. (1984). Decoupling of muonium in high transverse magnetic fields. *Physical review letters*, *53*(1), 90.

[Kim+21] Kim, C. U., Jung, E. D., Noh, Y. W., Seo, S. K., Choi, Y., Park, H., ... & Choi, K. J. (2021). Strategy for large-scale monolithic Perovskite/Silicon tandem solar cell: A review of recent progress. *EcoMat*, *3*(2), e12084.

[Kum+15] Kumar, M., Dubey, A., Adhikari, N., Venkatesan, S., & Qiao, Q. (2015). Strategic review of secondary phases, defects and defect-complexes in kesterite CZTS–Se solar cells. *Energy & Environmental Science*, *8*(11), 3134-3159.

[Li+21] Li, X., Li, P., Wu, Z., Luo, D., Yu, H. Y., & Lu, Z. H. (2021). Review and perspective of materials for flexible solar cells. *Materials Reports: Energy*, *1*(1), 100001.

[Liu+20] Liu, F., Zeng, Q., Li, J., Hao, X., Ho-Baillie, A., Tang, J., & Green, M. A. (2020). Emerging inorganic compound thin film photovoltaic materials: Progress, challenges and strategies. *Materials Today*, *41*, 120-142.

[Luq11] Luque, A., & Hegedus, S. (Eds.). (2011). *Handbook of photovoltaic science and engineering*. John Wiley & Sons.

[Mar+21] Marinopoulos, A. G., Vilão, R. C., Alberto, H. V., Ribeiro, E. F. M., Gil, J. M., Mengyan, P. W., ... & Lord, J. S. (2021). Hydrogen states in mixed-cation CuIn (1− x) Ga x Se2 chalcopyrite alloys: a combined study by first-principles density-functional calculations and muon-spin spectroscopy. *Philosophical Magazine*, *101*(22), 2412-2434.

[Mcg+21] McGott, D. L., Muzzillo, C. P., Perkins, C. L., Berry, J. J., Zhu, K., Duenow, J. N., ... & Reese, M. O. (2021). 3D/2D passivation as a secret to success for polycrystalline thin-film solar cells. *Joule*, *5*(5), 1057-1073.

[Nag+95] Nagamine, K., Iwasaki, M., Shimomura, K., & Ishida, K. (1995). Method of probing inner-structure of geophysical substance with the horizontal cosmic-ray muons and possible application to volcanic eruption prediction. *Nuclear Instruments and Methods in Physics*

Research Section A: Accelerators, Spectrometers, Detectors and Associated Equipment, *356*(2-3), 585-595.

[Nic99] Nickel, N. H. (1999). *Hydrogen in semiconductors II*. Elsevier.

[NRE] National Renewable Energy Laboratory NREL. Best Research-Cell Efficiency Chart. url: https://www.nrel.gov/pv/cell-efficiency.htm

[Och+00] Ochoa, D., Houdré, R., Ilegems, M., Benisty, H., Krauss, T. F., & Smith, C. J. M. (2000). Diffraction of cylindrical Bragg reflectors surrounding an in-plane semiconductor microcavity. *Physical Review B*, *61*(7), 4806.

[Pat88] Patterson, B. D. (1988). Muonium states in semiconductors. *Reviews of Modern Physics*, *60*(1), 69.

[Pra97] Pratt, F. L. (1997). Repolarization of anisotropic muonium in orientationally disordered solids. *Philosophical magazine letters*, *75*(6), 371-380.

[Reg+21] Regmi, G., & Subramaniam, V. (2021). Introduction to photovoltaics and alternative materials for silicon in photovoltaic energy conversion. In *Sustainable Material Solutions for Solar Energy Technologies* (pp. 131-173). Elsevier.

[REN] REN21. 2023. Renewables 2023 Global Status Report Collection

[Sal+11] Salome, P. M. P., Malaquias, J., Fernandes, P. A., Ferreira, M. S., Leitão, J. P., Da Cunha, A. F., ... & Viana, E. R. (2011). The influence of hydrogen in the incorporation of Zn during the growth of Cu2ZnSnS4 thin films. *Solar Energy Materials and Solar Cells*, *95*(12), 3482-3489.

[Tan19] Tanaka, H. K. (2019). Japanese volcanoes visualized with muography. *Philosophical Transactions of the Royal Society A*, *377*(2137), 20180142.

[Var+18] Varley, J. B., Lordi, V., Ogitsu, T., Deangelis, A., Horsley, K., & Gaillard, N. (2018). Assessing the role of hydrogen in Fermi-level pinning in chalcopyrite and kesterite solar absorbers from first-principles calculations. *Journal of Applied Physics*, *123*(16).

[Vil+03a] Vilão, R. C., Alberto, H. V., Gil, J. M., Duarte, J. P., de Campos, N. A., Weidinger, A., & Yakushev, M. V. (2003). Hydrogen states in CuInSe2—a μSR study. *Physica B: Condensed Matter*, *340*, 965-968.

[Vil+03b] Vilão, R. C., Gil, J. M., Alberto, H. V., Duarte, J. P., de Campos, N. A., Weidinger, A., ... & Cox, S. F. J. (2003). Muon diffusion and trapping in chalcopyrite semiconductors. *Physica B: Condensed Matter*, *326*(1-4), 181-184.

[Vil+05] Vilao, R. C., Alberto, H. V., Duarte, J. P., Gil, J. M., Weidinger, A., de Campos, N. A., ... & Cox, S. F. J. (2005). Muonium spectroscopy in ZnSe: Metastability and conversion. *Physical Review B*, *72*(23), 235203.

[Vil+08] Vilao, R. C., Gil, J. M., Weidinger, A., Alberto, H. V., Duarte, J. P., de Campos, N. A., ... & Cox, S. F. J. (2008). Acceptor level of interstitial muonium in ZnSe and ZnS. *Physical Review B*, *77*(23), 235212.

[Vil+15] Vilão, R. C., Vieira, R. B. L., Alberto, H. V., Gil, J. M., Weidinger, A., Lichti, R. L., ... & Lord, J. S. (2015). Muonium donor in rutile TiO 2 and comparison with hydrogen. *Physical Review B*, *92*(8), 081202.

[Vil+17] Vilão, R. C., Vieira, R. B. L., Alberto, H. V., Gil, J. M., & Weidinger, A. (2017). Role of the transition state in muon implantation. *Physical Review B*, *96*(19), 195205.

[Vil+18] Vilão, R. C., Vieira, R. B. L., Alberto, H. V., Gil, J. M., Weidinger, A., Lichti, R. L., ... & Lord, J. S. (2018). Barrier model in muon implantation and application to Lu 2 O 3. *Physical Review B*, *98*(11), 115201.

[Vil+19] Vilão, R. C., Alberto, H. V., Gil, J. M., & Weidinger, A. (2019). Thermal spike in muon implantation. *Physical Review B*, *99*(19), 195206.

[Vil+23] Vilão, R. C., Alberto, H. V., Ribeiro, E. F., Gil, J. M., & Weidinger, A. (2023, March). Muonium reaction in semiconductors and insulators: The role of the transition state. In *Journal of Physics: Conference Series* (Vol. 2462, No. 1, p. 012056). IOP Publishing.

[Vil02] Vilão, R. C. D. E. S. (2002). Estudo das interacçoes do hidrogénio com defeitos estruturais em semicondutores do tipo calcopirite utilizando técnicas de muoes (Master's thesis).

[Vil22] Vilão, R. C. (2023). *Semicondutores e Nanoestruturas* (1° Ed.). Coimbra: Imprensa da Universidade de Coimbra

[Vio+22] Violas, A. F., Oliveira, A. J., Teixeira, J. P., Lopes, T. S., Barbosa, J. R., Fernandes, P. A., & Salomé, P. M. (2022). Will ultrathin CIGS solar cells overtake the champion thin-film

cells? Updated SCAPS baseline models reveal main differences between ultrathin and standard CIGS. *Solar Energy Materials and Solar Cells*, *243*, 111792.

[Wad+09] Wadia, C., Alivisatos, A. P., & Kammen, D. M. (2009). Materials availability expands the opportunity for large-scale photovoltaics deployment. *Environmental science & technology*, *43*(6), 2072-2077.

[Yok+10] Yokoyama, D., Minegishi, T., Jimbo, K., Hisatomi, T., Ma, G., Katayama, M., ... & Domen, K. (2010). H2 evolution from water on modified Cu2ZnSnS4 photoelectrode under solar light. *Applied physics express*, *3*(10), 101202.

.